WSB.*APP/PS1* mice develop age-dependent cerebral amyloid angiopathy, cerebrovascular deficits, and white matter damage, which are modified by humanized *APOE* alleles.

Kristen D. Onos[1*], Olivia J. Marola[1*], Asli Uyar[2], Kelly J. Keezer[1], Juan Antonio K. Chong Chie[3,4], Kevin Elk[1], Phillip Bohn[5], Abigail E. Cullen[6], Kierra Eldridge[3,4], Scott Persohn[3,4], Jonathan Nyandu Kanyinda[1], Heidi K. Kocalis[1], Jennifer D. Whitesell[5], Julie A. Harris[5], Paul Salama[4], Ashley E. Walker[6], Gregory Carter[1,2,7,8], Michael Sasner[1], Paul R Territo[3,4], and Gareth R Howell[1,7,8]

*Authors contributed equally

[1] The Jackson Laboratory, Bar Harbor, ME, 04609, USA.

[2] The Jackson Laboratory for Genomic Medicine, Farmington, CT, 06032, USA.

[3] Stark Neurosciences Research Institute, Indiana University School of Medicine, Indianapolis, IN, 46202, USA.

[4] Department of Medicine, Division of Clinical Pharmacology, Indiana University School of Medicine, Indianapolis, IN, 46202, USA.

[5] Allen Institute or Brain Science, Seattle, WA, 98109, USA.

[6] Department of Human Physiology, University of Oregon, Eugene, Oregon, 97403, USA.

[7] Graduate School of Biomedical Sciences, Tufts University, Boston, MA, USA.

[8] Graduate School of Biomedical Sciences and Engineering, University of Maine, Orono, USA.

Corresponding author: gareth.howell@jax.org

Keywords: Alzheimer's disease and related dementias, vascular deficits, cerebral amyloid angiopathy, WSB

Abstract

Vascular contributions are now widely accepted to play a key role in many cases of dementia, including Alzheimer's disease (AD), that commonly manifest as cerebral small vessel diseases, including cerebral amyloid angiopathy (CAA). However, the mechanisms by which vascular contributions such as CAA contribute dementias such as AD are not well understood. This is due in part to the lack mouse models that develop robust CAA, hampering our ability to develop therapies that target vascular deficits. To address this, we have explored the use of distinct genetic contexts to enhance the face validity of mouse models for AD. We have previously identified the WSB/EiJ (WSB) strain as a model that shows increased susceptibility to CAA in the presence of the *APP/PS1* amyloid driver, compared to the commonly used C57BL/6J (B6) strain. Here, we now perform an in-depth characterization of WSB.*APP/PS1* and its WSB wild type (WT) counterpart, assessing male and female mice, at 4, 8, and 12 months of age (M). We show that WSB.*APP/PS1* mice show mild CAA at 8M, with robust CAA being apparent at 14M. Transcriptional profiling showed strong correlation to AMP-AD gene expression modules highlighting the human relevance of WSB.*APP/PS1* mice and predicted white matter deficits at 14M that was confirmed by immunofluorescence. PET/CT showed blood flow and metabolic deficits, and modifications in small vessel morphology in 8M WSB.*APP/PS1* compared to WSB WT mice. We tested whether cerebrovascular reactivity deficits in WSB WT mice may underly the susceptibility to CAA, but interestingly, they did not show age-dependent decline in reactivity that was observed in B6 mice. Finally, using an allelic series of humanized apolipoprotein E (*APOE*), we show that *APOE4* increased the extent of CAA in WSB.*APP/PS1* mice, compared to *APOE2* and *APOE3*, but in a sex-dependent manner. Collectively, these data show the utility of the WSB strain to uncover mechanisms of vascular contributions to Alzheimer's disease and related dementias.

Introduction

Alzheimer's disease and related dementias (ADRD) significantly impact quality of life and the ability to provide self-care. Current global estimates of incidence suggest that the 50 million people living with dementia will grow to exceed 152 million by 2050. Age is the greatest risk factor and interacts with genetic and environmental factors to increase risk for AD(*1*). AD is classically defined as the presence of specific pathology in the brain: deposition of amyloid, intracellular neurofibrillary tangles of Tau, neuroinflammation and neurodegeneration. Diagnosis is difficult as there are currently few reliable biomarkers. More recently, vascular contributions are considered hallmarks of most ADRD, including a common but often ignored pathology, namely deposition of insoluble amyloid beta in the cortical vessels and in the leptomeningeal arteries, referred to as cerebral amyloid angiopathy (CAA). CAA is present in up to 90% of AD patients(*2*), and is associated with endothelial cell dysfunction, hypoperfusion, production of reactive oxygen species (ROS), neurovascular damage, impaired clearance, and neurovascular uncoupling(*3, 4*). CAA is also one of the most common risk factors for lobar intracerebral hemorrhages and ischemia in the aging population(*5*). Changes in cerebral blood flow, vascular function, and subsequent metabolic dysregulation are detected in early stages of ADRD(*3, 4*), thought to occur prior to the development of CAA. However, despite the importance of vascular contributions to ADRD, the underlying causes of CAA are not well understood. Critically, it will be vital to decipher the underlying mechanisms behind vascular deficits in ADRD, in order to develop therapeutics that aim to improve vascular health and prevent cognitive decline.

Despite previous work focused on understanding vascular deficits in ADRD, and particularly in CAA, advances have been hampered by the lack of translationally relevant animal models(*6*). For instance, the widely used transgenic amyloid model mouse models, such as the 5xFAD or *APP/PS1*, phenocopy parenchymal plaque deposition but lack robust CAA even at older ages (*6*). We posit this is due in part to the limited genetic contexts that is inherent in classically used mouse strains – with the most commonly used strain being C57BL/6J (B6)(*6*). Recent work from our lab has taken advantage of wild-derived mouse strains(*7-9*). For example, WSB/EiJ (WSB) is a wild-derived mouse strain that was first established by wild mice trapped in Maryland that were sent to The Jackson Laboratory in 1986 and then inbred(*8*). This means that the genomes of these mice are specifically of the sub-species *Mus musculus domesticus*, and critically, exhibit natural genetic

variation believed to be important for the understanding of aging and diseases with complex etiology that engage multiple physiological systems(*10, 11*). By contrast, the commonly used laboratory strains, including B6, were generated through random crosses of European and Asian fancy mouse stocks, and have a heterogenous mixture of genomic contributions from all three *Mus musculus* subspecies(*11*). To study the utility of WSB for modeling ADRD, the *APP/PS1* transgenes were previously backcrossed from B6 to WSB for at least 10 generations (*8*). This initial characterization was performed after seven generations and ADRD phenotypes assessed at 8 months of age(*8*). At this age, in comparison to the commonly used B6.*APP/PS1*, WSB.*APP/PS1* exhibited lower numbers of parenchymal amyloid plaques, but significantly more cerebral amyloid angiopathy (CAA)(*8*). Cortical and hippocampal neuronal counts revealed moderate cell loss in both regions in female WSB.*APP/PS1* in comparison with non-carrier littermate controls(*8*).

Here, we now describe an extensive characterization of WSB.APP/PS1 mice, focusing particularly on cerebrovascular phenotyping. Collectively, our data show WSB.*APP/PS1* mice are susceptible to vascular deficits observed in human ADRD, including CAA and changes to cerebral blood flow and metabolism. The extent of CAA is modified by humanized APOE alleles (*APOE2*, *APOE3*, *APOE4*). We propose these strains as important preclinical models to uncover mechanisms and test novel therapeutics to treat vascular deficits in ADRD.

MATERIALS AND METHODS

Mouse strains and husbandry

All experiments were approved by the Institutional Animal Care and Use Committee at The Jackson Laboratory (JAX), Indiana University (IU), Allen Brain Institute (ABI), or University of Oregon (UO). WSB.*APP/PS1* mice (JR#33567283) were created as described previously(*8*), with all experiments utilizing the *APP/PS1* allele in the hemizygous state. The allelic series of humanized *APOE* was created by backcrossing either *APOE4*, *APOE3*, or *APOE2* (created by MODEL-AD)(*12*), to WSB for at least 6 generations. All experiments utilized humanized *APOE* alleles in the homozygous state. B6 mice were obtained from the Howell lab colony.

All cohorts of mice were bred and aged in the Howell lab mouse facilities at JAX, maintained in a 12/12-hour light/dark cycle and room temperatures were maintained at 18-24°C (65-75°F) with 40-60% humidity. All mice were housed in positive, individually ventilated cages (PIV). Standard autoclaved 6% fat diet, (Purina Lab Diet 5K52) was available to the mice *ad lib*, as was water with acidity regulated from pH 2.5-3.0. Cohorts of mice were either assessed at JAX or shipped to IU for PET/CT imaging, to ABI 3D vessel labeling, or to UO for assessment of cerebral artery reactivity/stiffness.

Immunofluorescence, imaging and analysis

Tissue collection

Mice were anesthetized with a lethal dose of tribromoethanol (800mg/kg) and were transcardially perfused with PBS. Brains were removed from the skull and hemisected. Hemibrains were placed in 4% PFA overnight at 4 degrees C, 15% sucrose overnight at 4 degrees C, and 30% sucrose overnight at 4 degrees C. Hemibrains were frozen and stored at -80 degrees C. Coronal 25µm sections were collected and stored floating in 31.25% glycerol, (Sigma-Aldrich, G5516-1L) 31.25% ethylene glycol (Sigma-Aldrich, 102466) dissolved in PBS at 4 degrees C.

Immunofluorescence

Brains sections were washed in PBS, permeabilized with 1% TritonX (Sigma-Aldrich, T8787) dissolved in PBS. Brains assayed for amyloid plaques were incubated in 40 µg/mL X34 (Sigma-

Aldrich, SML1954) dissolved in 40% ethanol, followed by washes in water and .02M NaOH. Brains were blocked in 5% normal donkey serum (Sigma-Aldrich, D9663) in 1% TritonX PBS for one hour at room temperature. Sections were incubated with primary antibody diluted in blocking solution overnight at 4 degrees C. Primary antibodies used included rabbit anti-IBA1 (Wako, 019–19741, 1.67µg/mL), rat anti-Clec7a (Invitrogen, mabg-mdect-2, 1:30), chicken anti-myelin basic protein (Invitrogen, PA1-10008, 3µg/mL), goat anti-IBA1 (Abcam, ab5076, 5µg/mL), and rat anti-CD68 (Bio-rad, MCA1957, 5µg/mL). Sections were washed in 2% TritonX PBS and incubated in secondary antibodies diluted in 2% TritonX PBS for 2 hours at room temperature. Secondary antibodies, and nuclei visualization by DAPI were as described previously(*13, 14*). Sections were mounted onto microscope slides with fluorescent mounting medium (Polysciences, 18606-20). Entire brain sections were imaged at 20x magnification using a Leica DMi8 microscope. All microscope settings were kept identical for each experiment. Images were stitched together in FIJI. Representative ROIs were maximum projections from 25 1µm confocal images taken with an inverted Leica confocal SP8 microscope.

Image analysis, CAA grading, and parenchymal plaque quantification

CAA grading was adapted from grading of human sections utilized by the Mayo clinic, where a section received a score of 0 if there was no CAA at all, and 0.5 if there was only leptomeningeal CAA. A section received a score of 1 if there was leptomeningeal CAA and scattered CAA in cortical vessels. A section received a score of 2 if there was leptomeningeal CAA and strong banding of CAA in cortical vessels, and a score of 3 if strong vessel banding was widespread throughout the cortex. For image quantifications, analyses were performed on three coronal brain sections per brain; at approximately bregma -1.955mm, -2.46mm, and -2.88mm. Scores from each of three brain sections were averaged to give the final CAA score for each brain.

Semi-automated plaque quantifications were performed on the same sections as those graded for CAA, using custom FIJI scripts. Brain cortexes were outlined manually using the polygon tool. The cortex ROI was shrunken by 50µm to avoid confounds at the tissue boarder. X34 stained images were subjected to a gaussian blur (sigma = 15) and were thresholded using the triangle method(*15*). Holes were filled and particles 10-50000µm^2 (an outline slightly larger than individual X34+ plaque areas) were added as ROIs. These ROIs were combined and overlayed

onto to the original X34-stained image. Regions within the combined ROI were thresholded using the MinError method and particles 100-50000µm^2 (X34+ plaques) were analyzed for area (plaque size) and were added as ROIs. X34+ cerebral amyloid angiopathy ROIs were manually removed. Number of particles (plaque number) was divided by the cortex ROI area to give X34+ parenchymal plaques/mm^2.

Plaque ROIs were expanded to give a 30µm ROI from the edge of the plaque. Overlapping expanded ROIs were combined into one ROI. Expanded ROIs were overlaid onto corresponding IBA1- and CLEC7A-assayed images. Regions within the expanded ROIs were thresholded using the triangle method, and all particles were analyzed for area. Total IBA1+ and CLEC7a+ area per brain section was divided by plaque number*plaque size in the corresponding brain section to quantify area per X34+ parenchymal plaque area.

RNA-Sequencing, and data processing

Left brain hemispheres were collected from male and female WSB.*APP/PS1* mice and wild-type (WT) littermate controls at 4, 8, and 14 months of age. Tissues were snap-frozen at the time of harvest and processed by the Genome Technologies Core at JAX for RNA extraction and library preparation as described previously(*16*). Libraries were sequenced in paired-end mode with a target of 40 million read pairs per sample. To ensure even sequencing depth and mitigate lane effects, samples were distributed across multiple flow cell lanes. FASTQ files were later concatenated per sample to produce a single paired-end file for downstream processing.

Raw sequencing reads were initially assessed for quality using FastQC (version 0.11.3, Babraham) and followed by quality-trimming and filtering using Trimmomatic tool (version 0.33) [Bolger 2014]. High-quality reads were then aligned to a custom *Mus musculus domesticus* (WSB/EiJ strain) reference genome using 'STAR' aligner (version 2.5.3). The custom genome for the WSB strain was created by integrating REL-1505 variants into the standard mm10 mouse genome. To enable detection of the human *APP/PS1* transgenes, we also appended sequences of *APP* and *PSEN1* to the reference genome and annotation files. Gene expression was quantified using two complementary approaches to support multiple downstream analytical methods: transcripts per million (TPM) using RSEM (version 1.2.31)(*17*) and raw read counts

using HTSeq-count (version 0.8.0)(*18*). Expression of *APP* and *PSEN1* transgenes was confirmed by inspecting RNA abundance in the engineered mouse model.

To reduce noise and improve statistical power, lowly expressed genes were filtered out by requiring a minimum total count across the samples. Genes with zero counts across all samples or have less than 10 reads in 3 or more samples were filtered out. For sex-adjusted analyses, genes located on the X and Y chromosomes were removed prior to PCA and DE modeling to avoid sex-chromosome-driven variation. Normalization and differential expression analysis were carried out using DESeq2, accounting for sex, age and genotype effects. Variance-stabilizing transformation (VST) was applied to normalized counts for downstream exploratory analyses and visualization. Principal Component Analysis (PCA) was used to assess sample-level clustering and detect potential outliers.

Functional enrichment analysis

Transcriptional profiling aimed to characterize genotype-associated transcriptional alterations across different ages in the WSB background. Analyses were stratified into three comparisons: genotype effect at 4, 8, and 14 months, based on sex-adjusted and sex-specific models. DESeq2 was used to identify gene expression differences between experimental groups, and the results were exported as log2 fold changes and associated statistics.

For each comparison, Gene Set Enrichment Analysis (GSEA)(*19*) was performed on pre-ranked gene lists (ordered by log2 fold change) using the gseGO(), gseKEGG(), and gsePathway() functions from the clusterProfiler and ReactomePA packages. Gene symbols were mapped to Entrez IDs via org.Mm.eg.db. Enrichments were computed separately for Biological Process (BP) Gene Ontology terms, KEGG pathways, and Reactome pathways. For exploratory analysis, significantly enriched pathways were defined based on normalized enrichment scores (NES) and adjusted p-values (< 0.2).

Selected biologically relevant pathways were visualized using customized gene-pathway network plots. For each pathway, core enriched genes identified by GSEA were mapped to their associated terms, allowing visualization of gene-level contributions within each module and experimental condition.

Mouse-human transcriptomic mapping

To evaluate the relevance of transcriptional changes in WSB mice to human AD, we utilized gene co-expression modules derived from the Accelerating Medicines Partnership for Alzheimer's Disease (AMP-AD) consortium. A total of 30 human brain co-expression modules were obtained from the Synapse data repository (SynapseID: syn11932957), originally constructed by Wan and colleagues(*20*) (2020) through a meta-analysis of differential gene expression across seven brain regions from three independent late-onset Alzheimer's disease (LOAD) cohorts (*21-23*). These modules were further clustered into five functional consensus groups representing major transcriptomic alterations in human late-onset AD.

We assessed the degree of concordance between genotype-driven expression changes in WSB mice and AMP-AD modules using a fold-change correlation approach(*24*). Specifically, we examined both sex-specific and sex-adjusted genotype effects at 4, 8, and 14 months of age, yielding multiple biologically distinct comparison groups. For each of these comparisons, Pearson correlation coefficients were calculated between the log2 fold-change values for mouse genes (relative to wild-type controls) and the corresponding log2 fold-change values observed in human AD cases versus controls. Human transcript-level fold-change data were obtained from the AD Knowledge Portal (SynapseID: syn14237651). Each AMP-AD module was assessed for concordance with each age- and sex-stratified genotype effect using the correlation coefficient and its associated p-value.

Results were visualized as module–condition correlation matrices plotted as bubble charts. Only significant correlations ($p < 0.05$) were shown with blue representing positive and red representing negative correlations. Circle size and color intensity reflected the magnitude of the Pearson correlation coefficient.

Assessment of mouse-human shared gene signatures

To further investigate the biological relevance of transcriptional overlaps between WSB mouse models and human AD, we focused on the subset of genes that contributed to significant correlations with AMP-AD modules ("intersecting gene sets"). These gene sets were extracted based on their similar differential expression pattern in both species.

Overrepresentation analysis (ORA) was performed using the enrichGO() function from the clusterProfiler R package to identify enriched GO-BP terms within these intersecting gene sets. The top enriched GO terms for each comparison–module pair were visualized using bar plots, ranked by adjusted p-value. These plots highlight biological processes most consistently altered across species. In addition, we performed GSEA using gseGO() for these intersecting genes ranked by log2 fold-change in mouse models. Results were visualized using split bar plots to display the top up- and down-regulated pathways (based on NES), with bar lengths proportional to NES and colored by gene set size. To capture the gene-level contributions to specific pathways, we constructed bipartite gene–pathway networks for top enriched terms (from GSEA) using the igraph package. Separate networks were generated for upregulated and downregulated pathways. Term and gene nodes were color-coded by directionality (e.g., red/green for up, blue/orange for down), and networks were visualized using force-directed layouts to aid interpretability.

PET/CT Imaging and Analysis

Evaluation of metabolism and perfusion was as described previously(*16*).

Radiopharmaceuticals: Regional brain glycolytic metabolism was monitored using 2-[^{18}F]-fluoro-2-deoxy-D-glucose (^{18}F-FDG), which was synthesized, purified, and prepared according to established methods, where unit doses (185 to 370 MBq) were purchased from PETNet Indiana (PETNET Solutions Inc). Brain perfusion was measured using Copper(II)-[^{64}Cu]-pyruvaldehyde-bis(N4-methylthiosemicarbazone) (^{64}Cu-PTSM), which was synthesized, purified, and unit doses (i.e. 370 to 740 MBq) dispensed by the PET Radiochemistry Core Facility at Washington University according to methods described previously(*25, 26*).

Positron Emission Tomography (PET) and Computed Tomography (CT) Imaging: To evaluate changes in cerebral glycolysis and cerebral perfusion mice were placed in a restrainer and consciously injected into the peritoneal cavity (^{18}F-FDG) or tail vein (^{64}Cu-PTSM) with 0.24-3.04 MBq of purified, sterile radiotracer, where the final volume did not exceed 10% of the animal's body weight. Each animal was returned to its warmed home cage and allowed 30 min (^{18}F-FDG) or 5 min (^{64}Cu-PTSM) to allow for uptake and cellular trapping(*26, 27*). Animals were fasted overnight only for imaging with ^{18}F-FDG. Post-uptake, mice were induced with 5% isoflurane gas

(95% medical oxygen), placed on the imaging bed, and anesthesia maintained at 1-3% isoflurane (97-99% medical oxygen) during acquisition, per our previous work(*16*). To provide both anatomical and function images, PET/CT acquisitions were performed with a Molecubes β-X-CUBE system (Molecubes NV, Gent Belgium), where calibrated list-mode PET images were acquired in list mode for 10 (^{18}F-FDG) or 20 (^{64}Cu-PTSM) min, and reconstructed into a single-static image using ordered subset expectation maximization (OSEM) with 30 iterations and 3 subsets(*28*). To provide anatomical reference and attenuation maps necessary to obtain fully corrected quantitative PET images, helical CT images were acquired with tube voltage of 50 kV, 100 mA, 100 µm slice thickness, 75 ms exposure, and 100 µm resolution. For β-CUBE studies, images were corrected for radionuclide decay, tissue attenuation, detector dead-time loss, and photon scatter previously described(*28*).

PET/CT Image Processing and Analysis: All PET/CT images were co-registered using a ridged-body mutual information-based normalized entropy algorithm(*29*) with 9 degrees of freedom and mapped to stereotactic mouse brain coordinates(*30*) using MIM Encore Software 7.3.2 (Beachwood OH). Study imaging and demographics data was managed using RedCap database hosted at Indiana University. Post-registration, 56 bilateral atlas regions were extracted, and left/right averaged to yield 27 unique volumes of interest that map to key cognitive, sensory, and motor centers. To permit dose, scanner and brain uptake normalization, Standardized Uptake Value Ratios (SUVR) relative to the cerebellum were computed for PET for each subject, genotype, age, and condition as follows:

$$SUVR(s, R, g, a, d) = \frac{R(s, g, a)}{C(s, g, a)} \quad (1)$$

where, s, g, a, R, and C are the subject, genotype, age, region/volume of interest, cerebellum region/volume of interest. The SUVR values were then converted to z-score as follows:

$$z\ score(s, R, g, a) = \frac{SUVR(s, R, g, a) - \bar{X}_R(R, g, a)}{\sigma_R(R, g, a)} \quad (2)$$

where, s, g, a, R, $\bar{X}_R$, and σ_R are the subject, genotype, age, mean of the reference population in SUVR, standard deviation of the reference population, based on the specified analytical strategies (effects of diet, aging, humanized genes, and AD-risk alleles). Data are then projected onto Cartesian space per our previous work(*4*), where the x-axis represents the z-score change in

perfusion, derived from the ^{64}Cu-PTSM data, and the y-axis is the z-score change in glycolytic metabolism(*31-33*) via ^{18}F-FDG.

To determine the radiotracer kinetics, arterial input function (C_a) were derived from whole blood measurements of ^{64}Cu-PTSM and were digitized and intensity normalized. At steady-state, ^{64}Cu-PTSM is trapped in the tissues directly proportional to tissue perfusion(*26*), where estimates of the tissue conductance is governed by the permeability-surface area product (PS) in a one tissue compartment model. Model estimates were determined using the autoradiographic approach(*27, 34, 35*), by solving the following partial differential equation:

$$\frac{dC_b}{dt}(s,R,g,t) = -C_a(t)PS \tag{3}$$

where, s, g, R, t, C_b, and C_a are the subject, genotype, region/volume of interest, time, concentration in the brain, and arterial input function. Estimates of PS were determined iteratively, using an average dose of 4.63 MBq and 2.8 ml average blood volume. Parameters were optimized via Levenberg-Marquardt algorithm using a sum-of-squares error of the absolute relative difference between the measured tissue tracer levels and estimated final value based on:

$$\Delta\varepsilon(s,R,g,t) = \left|\frac{C_m(t) - \bar{C}_b(t)}{\bar{C}_b(t)}\right| \tag{4}$$

where, $\Delta\varepsilon$, s, g, R, t, $\bar{C}_b$ and C_m are the absolute error difference, subject, genotype, region/volume of interest, time, average brain concentration, and modelled concentration, respectively. In all cases, trapezoidal quadrature was used to numerically integrated C_a with time using Eqn. 3, where a tolerance of 0.01 was used as the stopping criteria. The error estimate of this model was 0.95±0.033% with an averaged R^2 of 0.9984 across all subjects, genotypes, and regions.

3D Vessel Labeling, Imaging, and Quantification

To visualize vessels in WT and APP/PS1 WSB mice, mice were injected with DyLite as described previously(*36*). Tissue was harvested, sectioned and imaged as described previously(*36*). To provide quantification of vascular tree volume, exchange surface area and permeability, stacks of 140 32bit Red/Green/Blue/Alpha (RGBA) images were used to reconstruct a 3D volume using cubic spline interpolation, where the slice offset was based on the image section thickness (100µm). The 16-bit transformed green channel contained the information required to detect,

visualize, and extract 3D vessels. Post-reconstruction, image volumes were registered to the Allen Common Coordinate Framework(*37*) permitting alignment to a common reference space.

Due to the variance between voxel intensity values and subjects, a method to automatically normalize and detect the precise range of vessel values was developed and utilized the entropy of the volume for different ranges of voxel intensities that spanned from 0 to 65535. Data plotted as entropy vs. intensity range were used to determine the point where the entropy curve starts to decrease (i.e. $\Delta>0.01$), which was selected as the minimum of the threshold range. This threshold is used to obtain a coarse initial segmentation of the vessels' volume. Then, to establish the 3D connection between vessels, we used a 26-neighbors connected components process to reduced spurious voxels in the image volume that were not part of the vascular tree.

Once the vessels were extracted, the vascular tree was skeletonized by applying the medial axis transform(*38*), thus providing a midline throughout the entire tree that could be used for additional processing. This process facilitated the counting of the number of vascular branches, since the process was reduced to finding the locations where the vessels split, and branches are defined as a segment, or connected voxels, between two splitting locations. To perform this task, the algorithm started at any voxels that belong to the skeletonized vessels' tree, then traverses the complete tree until all voxels are explored via a divide and conquer approach. Traversing the vessels tree was defined as following the path of connected voxels and enumerating each voxel where the path divides. To prevent the algorithm from cycling infinitely, our method keeps track of which voxels were visited during this process.

To evaluate the vessel diameters for each branch, the algorithm iterated across all detected branches, and was fitted with a polynomial along the branch voxels to permit interpolation of elements. A normal vector between consecutive voxels of the fitted curve was used to obtain an orthogonal plane placed between the voxels being evaluated. Using the orthogonal plane and the normal vector, a 2D slice projection of the vascular tree was generated. In combination with the completed vascular tree, a ray casting process is used to calculate the vascular exchange surface (perimeter of the slice) and cross-sectional areas assuming a prolate ellipsoid, where origin of the ray was centered along the midline, and the ray in each direction intersects the vessel contour 180

out of phase. This process is repeated iteratively by rotating the angle between rays over the interval of 0° to 180° with 1° steps. The algorithm returns a set of measurements for each voxel in the skeletonized vessel tree.

Cerebral artery reactivity

Vasodilation and vasoconstriction responses were assessed *ex vivo* in isolated, pressurized posterior cerebral arteries, as described in detail(*39, 40*). Briefly, arteries were excised from the brain and placed in pressure myograph chambers (DMT Inc., Hinnerup Denmark) with physiological salt solution containing 145 mM NaCl, 4.7 mM KCl, 2 mM $CaCl_2$, 1.17 mM $MgSO_4$, 1.2 mM NaH_2PO_4, 5.0 mM glucose, 2.0 mM pyruvate, 0.02 mM EDTA, 3.0 mM MOPS buffer, 10 g/L BSA, 7.4 pH at 37°C. The arteries were then cannulated onto glass micropipettes and secured with nylon (11-0) sutures. Once cannulated, arteries were warmed to 37°C, pressurized to 50 mmHg, and equilibrated for approximately 1 hour. All arteries were submaximally preconstricted with phenylephrine (1-6 μM to obtain ~15-40% preconstriction). To measure vascular reactivity, changes in lumen diameter were measured in response to increasing concentrations of endothelium-dependent vasodilator acetylcholine ($1x10^{-9}$ to $1x10^{-4}$ M), endothelium-independent vasodilator sodium nitroprusside ($1x10^{-10}$ to $1x10^{-4}$ M), or vasoconstrictor endothelin-1 ($1x10^{-11}$ to $1x10^{-7}$ M). Acetylcholine dose responses were repeated after incubation with L-N^G-nitro arginine methyl ester (L-NAME, 0.1 mM for 30 minutes) to examine the contribution of nitric oxide synthase to endothelium-dependent vasodilation.

Cerebral artery stiffness

Passive arterial stiffness was measured *ex vivo* in the posterior cerebral artery by the resulting lumen diameter and medial wall thickness following increasing intraluminal pressure(*39*). Arteries were isolated and cannulated between glass pipette tips as described in Cerebral Artery Vasoreactivity. Passive stiffness was measured in arteries following 60-minute incubation in a calcium-free solution to eliminate the effects of myogenic tone. Measurements for each artery were recorded from 5 to 100 cmH_2O (3.7–73.5 mmHg) in 5 cmH_2O increments. Stress-strain curves were created for each artery to calculate β-stiffness. Stress was calculated as: $\sigma = PD/2WT$, where P is pressure in dyne cm^{-2}, D is lumen diameter and WT is wall thickness. Strain was calculated as: $\varepsilon = (D - D_i)/D_i$, where D_i is the initial lumen diameter. Data for each artery were fit to the curve:

$\sigma = \sigma_i e^{\beta\varepsilon}$, where σ_i is the initial stress (at 5 cmH_2O), and β is the slope of tangential elastic modulus versus stress. A higher β-parameter represents a stiffer artery.

Statistical analysis

Data were analyzed using GraphPad Prism9 software. Power calculations were performed before experiments were conducted to determine appropriate sample size. Data from experiments designed to test differences between two groups were subjected to an *F* test to compare variance and a Shapiro–Wilk test to test normality to ensure appropriate statistical tests were utilized. Fig. 1E(male), F, G; Fig. 3C, D; Fig. 4D; Fig. 5B, C, D were analyzed using unpaired two-tailed *t* tests. Fig. 1D(males); Fig. 1E(females) was analyzed using Welch's *t* test. Fig. 6B was analyzed using Mann-Whitney U tests. Data from experiments designed to test differences among more than two groups across one condition were subjected to a Brown-Forsythe test to compare variance and a Shapiro–Wilk test to test normality to ensure an appropriate statistical test was utilized. Fig. 7C, E(females), F, G(females) were analyzed using a one-way ANOVA with Tukey's post-hoc test. Fig. 1D(males), 7D were analyzed using a Kruskal–Wallis test with Dunn's post hoc test. Fig. 1D(females) was analyzed using a Brown-Forsythe ANOVA with Dunnett's T3 multiple comparisons test. Data from experiments designed to detect differences among multiple groups and across two conditions (Fig. 4C; Fig. 6D, F) were analyzed using a two-way ANOVAs. Data from experiments designed to test differences between two groups across multiple conditions (Fig. 6A, C) were analyzed with a three-way ANOVA.

For these statistical tests, every possible comparison was made, and multiplicity adjusted *P* values are reported. In all cases, data met the assumptions of the statistical test used. *P* values < 0.05 were considered statistically significant. Throughout the manuscript, results are reported as mean ± standard error of the mean (SEM).

RESULTS

We have previously shown WSB.*APP/PS1* develop cognitive deficits working memory as determined in the spontaneous alternation assay, limited but significant neuronal cell loss, and increased CAA compared to B6.*APP/PS1* mice, suggesting the WSB genetic context is more conducive to study the vascular contributions to ADRDs. Therefore, we first set out to better characterize the WSB.*APP/PS1* strain, focusing particularly on the anatomy and function of the cerebral vasculature.

WSB.APP/PS1 develop human-relevant CAA

To characterize CAA in WSB.*APP/PS1* mice, 4-, 8-, and 14-month-old (M) female and male WSB and WSB.*APP/PS1* mice were evaluated for CAA and parenchymal plaque deposition (**Fig. 1**). At 4M, hardly any X34+ parenchymal plaques were observed, and no vascular X34+ CAA was observed in either sex or genotype. Both male and female WSB.*APP/PS1* mice developed increasingly severe CAA (**Fig. 1C**) and parenchymal plaque deposition (**Fig. 1D**) at 8 and 14M. Consistent with human AD, female WSB.*APP/PS1* mice appeared to have more plaque deposition than their male counterparts. Plaque size remained consistent with age for each sex (**Fig. 1E**).

Previous studies have been demonstrated that microglial activity modifies CAA and parenchymal plaque development in mice(*41*). Moreover, we have previously shown WSB mice have fewer microglia compared B6(*8*). Furthermore, WSB microglia were shown to respond differently to amyloid with the *APP/PS1* transgenic driver(*9*). Therefore, plaque-associated microglial (IBA1+) and CLEC7a+ (a known disease-associated microglial protein) area was measured within the 30µm radius from each X34+ parenchymal plaque, to establish the role of microglia driven amyloid clearance. As anticipated, there was robust IBA1+ and CLEC7a+ expression in proximity to X34+ parenchymal plaques, and this expression remained consistent across ages and sexes (**Fig. 1F, G**).

Neuronal, vascular, and immune-related transcriptional changes emerge progressively in WSB.APP/PS1 mice

Transcriptomic profiling of brain tissues from male and female *APP/PS1* and WT WSB mice at 4, 8, and 14M revealed distinct temporal patterns in biological pathways as early as 4M (**Fig. 2A**),

well before overt amyloid plaque deposition is expected in *APP/PS1* models. At this early stage, enriched pathways were dominated by neuron projection organization and regulation of synaptic plasticity, with upregulation of genes such as *Xlr3b*, *Kdr* and *Rims1*. *Kdr* encodes VEGFR2, a major endothelial growth factor receptor essential for neurovascular coupling and angiogenesis, and its early upregulation may signal adaptive vascular remodeling in response to subtle perfusion stress. Upregulation of *Rims1*, a presynaptic scaffolding protein, supports neurotransmitter release and short-term synaptic plasticity, suggests early compensatory remodeling of neuronal circuits. These neuronal changes are accompanied by transcriptional signatures of glial cell activation, indicating that neuroinflammatory processes are initiated prior to detectable amyloid pathology in WSB.*APP/PS1*. Notably, genes related to response to starvation and the endoplasmic reticulum unfolded protein response were downregulated, both processes including decrease in *Xbp1* and *Hspa5* genes. *Xbp1* is a master transcription factor in the ER stress response and regulated metabolic adaptation to nutrient limitation(*42*), while *Hspa5* encodes a central ER chaperone maintaining protein folding homeostasis. Such suppression has been reported to precede overt protein aggregation, potentially impairing the ability of neurons and vascular cells to buffer misfolded proteins and contributing to vulnerability in preclinical AD stages. Chronic low-level ER stress has been implicated in promoting vascular endothelial dysfunction via oxidative stress and inflammatory signaling. In this context, early molecular changes in nutrient-sensing and proteostatic pathways could represent an upstream trigger for the vascular and inflammatory signatures observed at later ages.

By 8M, the transcriptional profile shifted toward a strong vascular–immune axis (**Fig. 2A**). Significant enrichment was observed in pathways increasingly recognized as central to CAA and small vessel disease in AD, such as extracellular matrix organization, complement and coagulation cascades, and cell surface interactions at the vascular wall. Among the upregulated genes, *Itgax* marks a subset of activated microglia enriched in neurodegenerative contexts, while *Flt1* mediates vascular inflammation and blood-brain barrier dysfunction. These signatures, coupled with downregulation of aerobic respiration and oxidative phosphorylation, point to a convergence of vascular injury, metabolic compromise, and immune activation, consistent with core features of CAA-associated pathology in AD.

At 14M (**Fig. 2A**) transcriptional changes were dominated by microglial activation and phagocytic clearance. Enriched immune pathways included cell killing (*Tyrobp*, *B2m*, *Clec7a*, *Lyz2*, *Ptprc*) and phagosome (*Ctss*, *Clec7a*, *Fcgr3*, *Itgb2*, *Rab7b*). *Tyrobp* is a core hub in TREM2-dependent microglial activation networks in AD(*43*), while *Clec7a* marks disease-associated microglia clustered around amyloid deposits. The upregulation of these pathways and genes is consistent with sustained neuroinflammation and heightened immune-mediated clearance activity in advanced amyloid disease.

Overall, the temporal cascade in WSB.*APP/PS1*, beginning with early neuronal plasticity changes at 4M, progressing through vascular and extracellular matrix remodeling at 8M, and culminating in immune–metabolic activation under high amyloid load at 14M, aligns with recent human and preclinical evidence supporting metabolic and vascular dysfunction as an early driver of downstream neurodegeneration in AD.

Correlation of WSB.APP/PS1 transcriptional profiles with human AMP-AD modules across age and sex

To evaluate the AD relevance of age- and sex-specific transcriptional changes in WSB.*APP/PS1*, we computed correlations between mouse differential expression profiles and 30 human AMP-AD co-expression modules (**Fig. 2B**). In terms of human age equivalence, 4, 8, and 14M mice roughly correspond to early adulthood (~20–30 years), middle age (~35–45 years), and late middle age to early elderly (~55–65 years) in humans, respectively(*44*). This framework enables interpretation of transcriptomic shifts in WSB.*APP/PS1* mice along a compressed timeline, mapping them onto the stages of AD pathophysiology observed in humans.

At 4M, correlations were generally modest, reflecting the limited overlap between early-stage molecular alterations in WSB.*APP/PS1* mice and the largely late-stage signatures represented in the AMP-AD cohort. Nonetheless, certain neuronal and metabolic modules exhibited weak but significant correlations, suggesting that subtle network remodeling and early metabolic shifts are already underway.

Correlations strengthened markedly for immune–microglial and vascular/ECM-related modules at 8M (**Fig. 2B**), consistent with the emergence of neuroinflammatory activation and cerebrovascular remodeling during mid-stage disease. These changes mirror the vascular amyloid deposition and immune cell recruitment characteristic of WSB.*APP/PS1* pathology. At the same time, significant but weak correlations start to emerge for neuronal, synaptic and glial modules in both positive and negative directions. This pattern likely reflects the complex cellular remodeling processes occurring at this stage.

By 14M (**Fig. 2B**), correlations with human AMP-AD modules became more pronounced and broadly distributed across multiple functional domains. The highest positive correlations were seen for consensus clusters A and B (modules enriched for extracellular matrix (ECM) organization, immune activation, and cytokine signaling) consistent with the pronounced vascular remodeling and neuroinflammatory signatures that dominate this late stage. Cluster D, spanning myelination, neuronal and glial development, and astrocyte biology, also showed significant positive correlations, indicating glial activation and changes in neuroglial support networks under sustained amyloid burden. Cluster C, representing synaptic signaling and broader neuronal system pathways, displayed more significant correlations in females than in males, with limited overlap between the sexes at the individual module level. This sex-biased divergence suggests that synaptic remodeling programs are differentially engaged in males and females during advanced disease. Finally, Cluster E, which includes cell cycle, DNA repair, and RNA metabolism modules, exhibited striking sex-specificity: correlations were in opposite directions between males and females, pointing to fundamentally different regulation of cell cycle and genome maintenance pathways in the aging mouse brain depending on sex.

Overall, the AMP-AD module mapping revealed distinct temporal trajectories in how WSB.*APP/PS1* transcriptional profiles align with human AD signatures. Vascular, immune, and extracellular matrix–related modules showed a progressive strengthening of positive correlations from mid- to late-stage disease, suggesting these processes represent a sustained and converging pathology. Myelination and astrocyte related modules became more prominent at later stages, while synaptic signaling modules displayed a marked sex bias, with stronger and more numerous correlations in females. The most striking sex specificity emerged in modules related to cell cycle,

DNA repair, and RNA metabolism, where the direction of correlation reversed between males and females. Collectively, these patterns highlight that the temporal evolution of molecular networks in WSB.*APP/PS1* mice is shaped both by disease stage and by sex, with some processes showing steady progression and others exhibiting divergent, sex-dependent trajectories.

WSB.APP/PS1 mice show human-relevant white matter damage

White matter damage is often a key indicator of cerebrovascular damage in human patients. Interestingly, the TCXyellow module from the consensus cluster D, representing myelination, neuronal and glial development, and astrocyte biology, showed strong positive correlations between WSB.*APP/PS1* sex-adjusted expression profiles at 14 months and human AD transcriptional changes (**Fig. 2B**). The key contributing genes driving the strong mouse–human correlation included *Spp1* and *Csf1* (key mediators of microglia–oligodendrocyte crosstalk and glial activation), *Cpq* and *Apod* (linked to lipid metabolism and myelin turnover), and *Nfe2l2* and *Itgb1* (stress response and extracellular matrix signaling) (**Fig. 2C, D**). This pattern suggests the human–mouse overlap reflects an integrated glial response involving astrocytic, microglial, and vascular-interacting pathways, potentially resulting in myelin changes in WSB.*APP/PS1* mice. To determine this, sections that included the corpus callosum and cortex from 14-month-old male and female WSB.*APP/PS1* and WSB control mice were stained with antibodies to visualize myelin (myelin basic protein, MPB, **Fig. 3**) and MBP intensity evaluated. Compared to WSB controls, WSB.*APP/PS1* showed a significant reduction in MBP intensity in the corpus callosum and cortex of male mice, with a trending reduction in female mice (**Fig. 3C, D**). Interestingly the reduction in MBP intensity appeared greater in male WSB.*APP/PS1* mice, which aligned with the stronger correlation of the TCXyellow module in male compared to female mice (**Fig. 2D**). Collectively, these data support human-relevant white matter damage in WSB.APP/PS1 mice.

WSB.APP/PS1 show vascular and metabolic uncoupling, increased vascular tree volume, surface area and permeability changes

To understand the relationship between cerebral blood flow (CBF) and metabolism, we performed regional neurovascular uncoupling analysis per our previous work(*4*). As anticipated, WSB.*APP/PS1* relative to WSB showed significant regional metabolic and vascular dysregulation

(MVD) (**Fig. 4A, B**), with most brain regions in both sexes showing prodromal (PD, ↑perfusion, ↑metabolism) or neuro-metabolic and vascular failure (NMVF, ↓perfusion, ↓metabolism) coupled phenotypes. In addition to these changes, WSB.*APP/PS1* mice (relative to male WSB WT) also show a divergent sexually dimorphic regional pattern. Male WSB.*APP/PS1* mice showed Type 1 uncoupling (T1U, ↑perfusion, ↓metabolism) in the agranular insular cortex (AI), ectorhinal cortex (ECT), and fornix, while the lateral orbital (LO), ventral orbital (VO), hippocampus (HIP), and prelimbic (PrL) showed Type 2 uncoupling (T2U, ↓perfusion, ↑metabolism) (**Fig. 4A, B**). Moreover, the dorsolateral-inferior-ventral entorhinal (DLIVEnt) and visual 1 and 2 (V1V2) cortices showed the PD phenotype, while the parietal association cortex (PtA) is in NMVF. By contrast, female WSB.APP/PS1 (relative to female WSB WT) mice showed significant T2U in temporal association cortex (TeA), parietal association cortex (PtA), and secondary sensory cortex (S2), while the Perirhinal Cortex (PRH) showed a PD phenotype (**Fig. 4A, B**). To understand if these sexually dimorphic patterns were related to changes in vascular permeability (P) and surface area (S) changes, we kinetically modeled the ^{64}Cu-PTSM images, yeilding regional PS product (ml/g.min) which is a measure of the tissue bulk permeability (**Fig. 4C, D**). As anticipated, female WSB.*APP/PS1* showed a significant increase in PS product (regions $p<0.001$), relative to WSB, across all brain regions; however, male mice did not show this same phenotype at the same age (**Fig. 4C**). Importantly, there was a sexual dimorphic effect in female WSB.*APP/PS1* (sex $p=0.019$), not observed in the males of the same genotype. To illustrate that this was a global effect, we computed whole brain regional changes, which also showed the same genotype and sex effect (**Fig. 4D**).

In an effort to decouple the bulk permeability changes from one another, we investigated if total vascular volume and/or exchange surface area changed with genotype and sex, through *in vivo* labeling of vessels by DyLight (**Fig. 5A**). Despite no differences in overall brain volume between genotypes (**Fig. 5B**), vascular tree volume was significantly different with genotype for both males and females (**Fig. 5C**). In addition, computing the exchange surface area (S), as the perimerter of the vessel cross-section, revealed that whole brain vascular S was also signficantly higher in WSB.*APP/PS1* mice than WSB (**Fig. 5D**), and was sexually dimorphic, with females retaining higher S compared to males of the same genotype. To understand if this S change was driven by the vessel size and how these were distributed, we computed histograms of all vessel diameters

across the entire vascular tree for both genotypes in females only (n=3/genotype) (**Fig. 5E, F**), since only females showed changes. Based on these results, female WSB.*APP/PS1* mice show a pronounced shift in vessel diameters, consistent with the formation of capillaries and meta-aterioles (**Fig. 5E**), and when expressed as a percentage, this showed that the vascular tree in this genotype increased the density of these vessels by ~2% over WSB in the small vessel range. To understand if these changes were associated with significant changes in exchange S across the vessel tree, we also computed histograms of exchange S for both genotypes, and displayed this as area (**Fig. 5E**) and and percentage (**Fig. 5F**). As with the vessel diameters, the distribution of the surface areas was shifted between WSB.APP/PS1 and WSB, with greater numbers of vessels with smaller S, consistent with the development of capillaries and meta-aterioles.

WSB vessels do not show age-dependent decline in vascular function and integrity

To better understand the functional cerebrovascular differences between strains, we performed ex vivo studies of posterior cerebral arteries from young and old B6 and WSB female mice. At young ages, there were no differences in the cerebral artery endothelium-dependent vasodilation, measured as the response to acetylcholine, between B6 and WSB mice (**Fig 6A, B**). Cerebral arteries from old B6 mice had significantly impaired endothelium-dependent vasodilation compared with arteries from young B6 (**Fig 6A, B**). In contrast, arteries from old WSB mice were not impaired, with endothelium-dependent vasodilation similar to that of young B6 and young WSB (**Fig 6A, B**). In all groups, the endothelium-dependent vasodilation to acetylcholine was almost entirely blocked by the nitric oxide synthase inhibitor L-NAME (**Fig 6A**), indicating that nitric oxide bioavailability was lower in old B6, but maintained in old WSB (**Fig 6A**). When examining the response to endothelium-independent vasodilator sodium nitroprusside, we found that all groups had similar responses (**Table 1**), demonstrating that smooth muscle cell responsiveness was not different between groups. The amount of artery preconstriction and maximal artery diameter were similar between groups (**Table 1**), indicating that these potential confounding factors did not impact the vasoreactivity measures. We also measured the ability of the posterior cerebral artery to vasoconstrict in response to endothelin-1(**Fig 6C, D**). We found that endothelin-1 vasoconstriction was not different between young B6 and young WSB mice. Arteries from old B6 mice vasoconstricted less to endothelin-1 than young B6 arteries (**Fig 6C, D**). In contrast, the endothelin-1 vasoconstriction was not different between young and old WSB

mice (**Fig 6C, D**). Thus, old WSB mice do not have the age-related declines in cerebral artery endothelial function and vasoconstrictor responsiveness that are present in old B6 mice.

We measured the passive stiffness of posterior cerebral arteries incubated in a solution free from calcium to remove any myogenic tone. We used the changes in lumen diameter and wall thickness in response to increasing pressure to create stress-strain curves (**Fig 6E**) and calculate β-stiffness. We found that old age led to stiffer cerebral arteries in both B6 and WSB mice compared with young mice (**Fig 6F**). In addition, there was a main effect of strain (2x2 ANOVA main effect p=0.021), such that WSB mice had stiffer cerebral arteries than B6 mice (**Fig 6F**). Thus, old age and the WSB strain are associated with stiffer cerebral arteries. Unlike the findings for vasoreactivity, the old WSB mice are not protected against the age-related increases in cerebral artery stiffness.

Humanized APOE alleles differentially modify CAA, plaque deposition, and plaque-associated microglial area in WSB.APP/PS1 mice.

The E4 allele of *APOE* (*APOE4*) allele is the most prominent risk allele for the development of late-onset Alzheimer's disease, with *APOE3* being a neutral allele, and *APOE2* being protective. *APOE4* is also known to increase severity of CAA in humans and mouse models. Therefore, to determine the effect of *APOE* status in the context of WSB-specific vascular deficits, a humanized *APOE* allelic series was backcrossed onto the WSB genetic background, and WSB.*APP/PS1.APOE2/2*, WSB.*APP/PS1.APOE3/3*, and WSB.*APP/PS1.APOE4/4* strains created. Male and female mice of each strain were aged to 8M and brain sections assessed for CAA and parenchymal plaques, as well as plaque-associated microglia as described previously (**Fig. 1**). Compared to WSB.*APP/PS1.APOE2*, WSB.*APP/PS1.APOE4* significantly increased CAA regardless of sex, whereas WSB.*APP/PS1.APOE3* showed significantly increased CAA in males, but not in females (**Fig 7A-C**). Observationally, using data presented in Figure 1, the degree of CAA in WSB.*APP/PS1* mice (mouse *Apoe*) appeared equivalent to WSB.*APP/PS1* mice carrying either *APOE2* or *APOE3* (**Fig. 7C**).

APOE genotype also significantly modified parenchymal plaque deposition in both males and females (**Fig. 7D**). In females, *APOE3* reduced parenchymal plaque deposition compared to

APOE2, and in males, *APOE4* had more parenchymal plaques compared to *APOE3*. APOE genotype did not significantly modify parenchymal plaque size in males or females (**Fig. 7E**). To investigate whether humanized APOE modulated plaque-associated microglial volume, IBA1+ microglia and CLEC7A+ area was measured within a 30µm radius from the edge of X34+ parenchymal plaques. Interestingly, *APOE4* genotype significantly increased plaque-associated microglial volume compared to *APOE2* in both males and females (**Fig. 7F**). *APOE3* genotype also significantly increased plaque-associated microglial volume compared to *APOE2* in females (**Fig. 7F**). Plaque-associated CLEC7a+ area was consistent across APOE genotypes regardless of sex (**Fig. 7G**). Therefore, compared to *APOE3* (neutral) or *APOE2* (protective), *APOE4* resulted in both increased CAA and parenchymal plaque-associated microglial volume.

DISCUSSION

AD is considered the most common form of dementia, and yet vascular anomalies, such as CAA, are present in the vast majority of cases. Despite this, the majority of mouse models relevant to AD, have focused on the primary AD pathologies, amyloid and tau. For instance, the commonly used transgenic-based 5xFAD and *APP/PS1* models, as well as the recently developed knock-in APP^{SAA} and NL-G-F models, at least on the B6 background, show small but significant amounts of CAA but generally at later ages(*36*). In mice, CAA has been studied using rare mutations that model CAA, such as the Dutch or Iowa mutations(*45*), although the pathophysiology in these cases are unlike clinical presentation seen in AD. The lack of co-occurrence between hallmark AD pathologies (amyloid and tau), and vascular anomalies (e.g., CAA) in commonly used mouse models has likely hampered our abilities to understand how they synergize to cause neurodegeneration and cognitive decline. In this study, we continue to show the value of non-traditional inbred mouse strains to study AD. We previously reported that WSB.*APP/PS1* showed significant levels of CAA and cognitive deficits at 8 mos(*8*), that correlated with differences in myeloid cell profiles(*9*). Here, we define the timeline of CAA development and show they have human AD-relevant neurovascular and metabolic uncoupling. We also use transcriptomics to define pathways perturbed throughout the disease course, including myelin deficits, and confirm this using immunofluorescence. Finally, we create an allelic series of humanized *APOE* in combination with *APP/PS1* on the WSB background and show that *APOE4* increased the degree of CAA.

PET/CT showed vascular and metabolic uncoupling occurs early in the disease course in WSB.*APP/PS1*. Multiple studies suggest changes to energy metabolism(*46-48*) and vascular health(*49, 50*), particularly in cerebral blood flow, occur prior to any signs of cognitive decline – suggesting these may be early drivers of AD. Clinical studies have demonstrated a reduction in glucose brain metabolism and cerebral blood flow disturbances in at-risk patient populations even before detectable levels of amyloid accumulation(*51-53*). Initially, blood flow may be increased in response to an energy deficit, as has been observed both preclinically and clinically. In response to blood flow disturbances, a strong angiogenic response can occur in order to counter the effects of low oxygen tensions, leading to an increase in vascular density(*54*). Arteriogenesis can also occur as it is driven by hemodynamic factors such as stretch and shear stress(*55*). Importantly,

disordered vascular remodeling and arteriovenous malformations, have been shown to can also lead to blood vessel rupture and organ hemorrhage. Interestingly, studies in stroke(*56, 57*) and traumatic brain injury(*58*) have shown that cerebral perfusion insufficiency results in a metabolic depression and concomitant hypoperfusion. Central to our hypothesis is that age-dependent reductions in cerebral blood flow lead to regional decreases in glycolytic metabolism.

Until recently, CAA has been largely absent in the majority of AD models. In WSB.*APP/PS1* CAA first appears between 4 and 8 mos, with the more significant CAA apparent by 14 mos, which coincides with the emergence and progression of parenchymal amyloid. To quantify CAA, we modified a method developed to grade CAA in human postmortem brains that was based on clinical scoring methods. The presence of CAA in the leptomeninges received the lowest score (score 0.5) with CAA in the penetrating cortical vessels increasing the CAA score based on the number of vessels affected (score 1-3). Although not quantified, the presence of CAA in WSB.*APP/PS1* showed regional variability across mice, with different cortical regions more or less affected. This aligns with human studies that show AD patients can show varying degrees of CAA, with certain cortical regions (e.g., occipital and parietal cortex) often most affected(*59*). Despite its effectiveness at relatively quickly and efficiently 'grading' CAA, improved quantification methods for CAA are needed, and machine-learning approaches are under devleopment by our group, with the intent to uncover the mechanistic drivers of CAA in WSB.*APP/PS1*. We anticipate the WSB strain harbors genetic factors that increase risk for CAA and possibly other vascular anomalies. Genetic mapping approaches – such as quantitative trait loci (QTL) mapping – can facilitate the identification of these factors. Interestingly, previous studies showed that genetic loci in the WSB strain modify outcome measures in a stroke model (*60*). Studies are underway using a B6/WSB F2 mapping population to identify the genetic factors that modify risk for CAA, and it will be interesting to compare them to those identified in the stroke model. Ultimately, these genetic factors will inform us about the mechanisms driving CAA in AD, and hopefully identify novel therapeutic avenues to explore to treat AD.

To begin to understand the mechanisms underlying vascular dysfunction in WSB.APP/PS1 mice, we tested age-related vessel function, contrasting young and old WT WSB with WT B6 mice. Our findings for lower endothelium-dependent vasodilation and endothelin-1-mediated

vasoconstriction in old B6 mice are consistent with the literature(*39, 61-64*). Consistent with previous studies, we also find that the impairment in endothelium-dependent vasodilation is due to reduced nitric oxide bioavailability(*39, 62, 63*). Previous studies have further demonstrated that increased reactive oxygen species are the primary driver of the lower nitric oxide bioavailability in old age(*40, 62*). Endothelin-1 also increases in the plasma and endothelial cells with age (*65*). It has been proposed that these higher levels of endothelin-1 cause vasoconstriction impairments due to desensitization(*66*). Importantly, these studies demonstrate that old WSB mice do not have the same impairments in vasodilation and vasoconstriction as old B6 mice. These are potentially mediated by lower oxidative stress and endothelin-1 in old WSB, which requires further investigation. Unlike the vasoreactivity measures, WSB cerebral arteries are vulnerable to age-related stiffening. The functional consequences of cerebral artery stiffening are not entirely clear. It is known that the age-related stiffening of large extracranial arteries is associated with cerebral artery dysfunction(*67, 68*), likely due to the resulting elevation in pulse pressure. However, it is unknown if the stiffness of the cerebral arteries affects their own vasoreactivity. Cerebral arteriole stiffness is also related to impaired glymphatic function(*69*), a potential pathway for Aβ clearance from the brain(*70*). Thus, the greater cerebral artery stiffness in the WSB mice could impact Aβ clearance, an area warranting further study.

Vascular deficits have only more recently been appreciated as critical contributors to many dementias, including AD, mixed (etiology) dementia, Parkinson's disease and others. Vascular deficits include a variety of pathologies including CAA, blood flow deficits, lacunar infarcts and small vessel disease (SVD). Mechanisms underlying vascular contributions to cognitive decline and dementia (VCID) are not well understood, and this may be contributing to the lack of success in clinical trials for particularly AD. Few if any clinical trials are focusing on vascular pathologies (*71*). In addition, current anti-amyloid-based treatments increase risk for amyloid-related imaging abnormalities (ARIA), that are thought to be as a result of cerebrovascular deficits(*72*). The presence of APOE4 significantly increases risk of ARIA, possibly due to the increased CAA(*72*). Given the need to develop strategies to treat VCID and ARIA, improved mouse models that recapitulate these key features are essential. We propose incorporation of WSB genetic context into mouse models will improve the translatability of the next generation of ADRD mouse models. To this end, WSB.*APP/PS1* are available from the JAX repository (#33567283) and the APOE

allelic series on WSB are available upon request to the corresponding author. In addition, the IU/JAX/PITT MODEL-AD (Model Organism Development and Evaluation for Late-onset AD) center is including WSB as a second genetic context in its collection of LOAD mouse models. MODEL-AD is charged with creating preclinical mouse models to improve the translatability of preclinical studies to the clinic(*73*). Models incorporate aging as well as genetic and environmental risk factors to recapitulate the complexity of human LOAD. Although models are standardized on the B6 background, a subset of those models is being generated on the WSB background, incorporating *APOE4*, in combination with WT and mutant humanized Aβ and *MAPT* alleles. All models as well as all associated phenotyping data are being made available at the earliest opportunity.

In summary, we show that, unlike previously published B6.*APP/PS1*, WSB.*APP/PS1* mice develop CAA, and white matter damage between 4-14 mos. Vascular/metabolic uncoupling is apparent at 8 mos. Similar to human studies, CAA is modified by humanized APOE alleles, and collectively these data further support the use of the WSB strain, rather than B6, to uncover mechanisms underlying VCID and the development of new treatments.

ACKNOWLEDGEMENTS/CONFLICTS/FUNDING SOURCES

We are grateful to JAX Scientific services, particularly Genome Technologies, and Transgenic Genotyping Services. This work was funded by U54-AG054345, U54-AG054349 and R21-AG078575-01. GRH holds the Diana Davis Spencer Foundation Chair for Glaucoma Research.

FIGURES AND TABLES

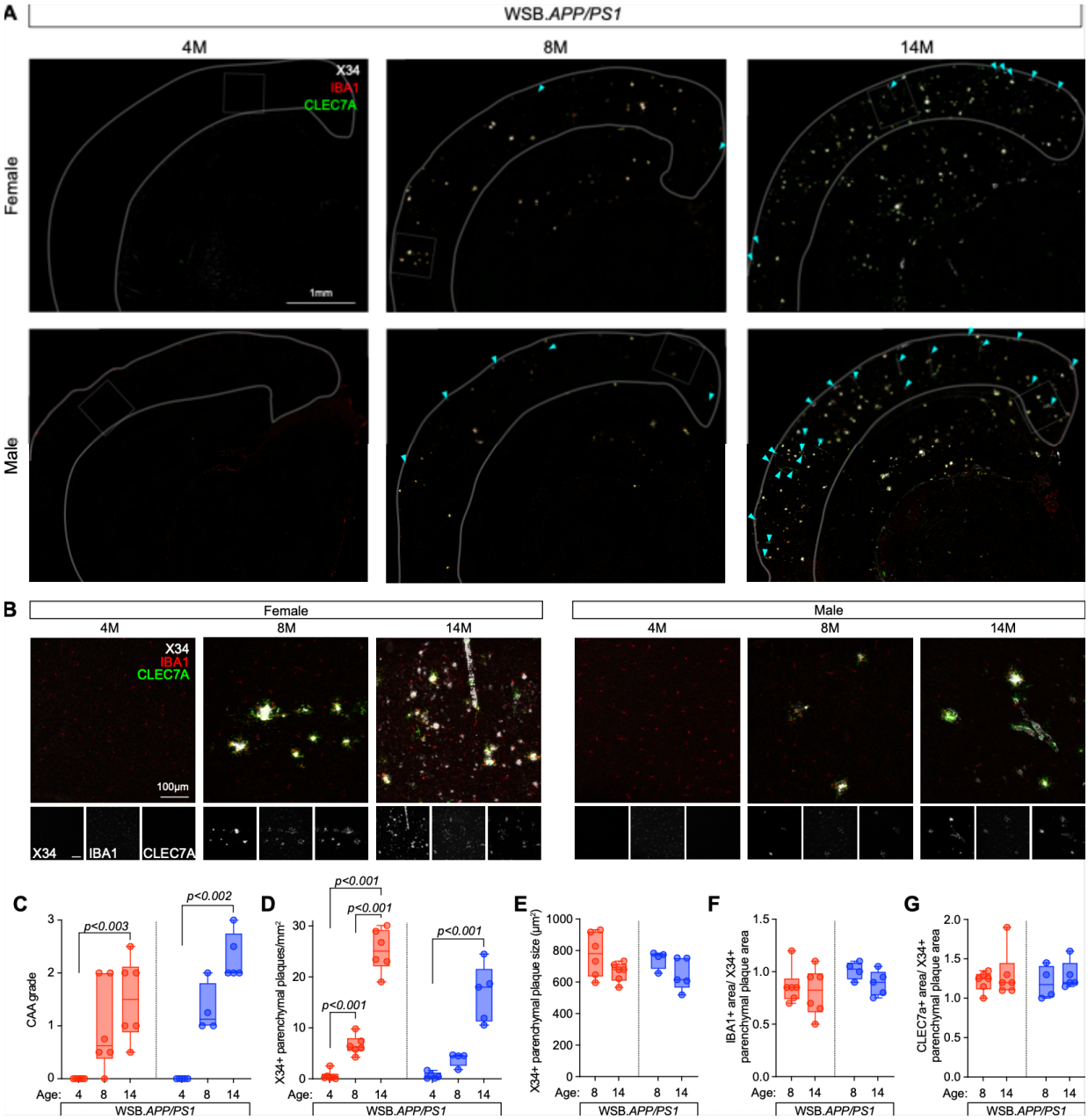

Figure 1: CAA and parenchymal plaque characterization in WSB.APP/PS1 mice

(A) Female and male 4M, 8M, and 14M WSB.*APP/PS1* brain hemisections stained with X34 (white) and immunoassayed for IBA1(red) and CLEC7a (green). Arrowheads indicate CAA. **(B)** High-resolution insets of representative parenchymal plaques and CAA. Individual images of X34, IBA1, and CLEC7a are shown below the merged image. **(C)** Quantification of CAA scores. CAA scores significantly increased with age in both sexes ($p<0.001$, Kruskal-Wallis tests, Dunn's multiple comparisons test). **(D)** Cortical parenchymal X34+ plaque quantifications

normalized to cortical area. Both male and female WSB.*APP/PS1* had increased parenchymal plaque deposition with age (Female: $p<0.001$, Brown-Forsythe ANOVA test, Dunnett's T3 multiple comparisons test; Male: $p<0.001$, Kruskal-Wallis test, Dunn's multiple comparisons test). **(E)** Average plaque size quantifications. No differences were observed in either sex across ages (Female: Welch's t-test, $p=0.107$; Male: two-tailed t-test, $p=0.146$). **(F)** Average IBA1+ area and CLEC7A+ area **(G)** normalized to average plaque size. No differences were observed across age for IBA1 ($p=0.629$ and $p=0.129$ for female and male respectively, two-tailed t-tests) or CLEC7A+ area (Female: $p=0.831$, Mann-Whitney test; Male: $p=0.514$, two-tailed t-test). For 4M, 8M, and 14M, respectively; female: n=6, 6, 6; male: n=5, 4, 5. Female data indicated in red, male data in blue (C-G).

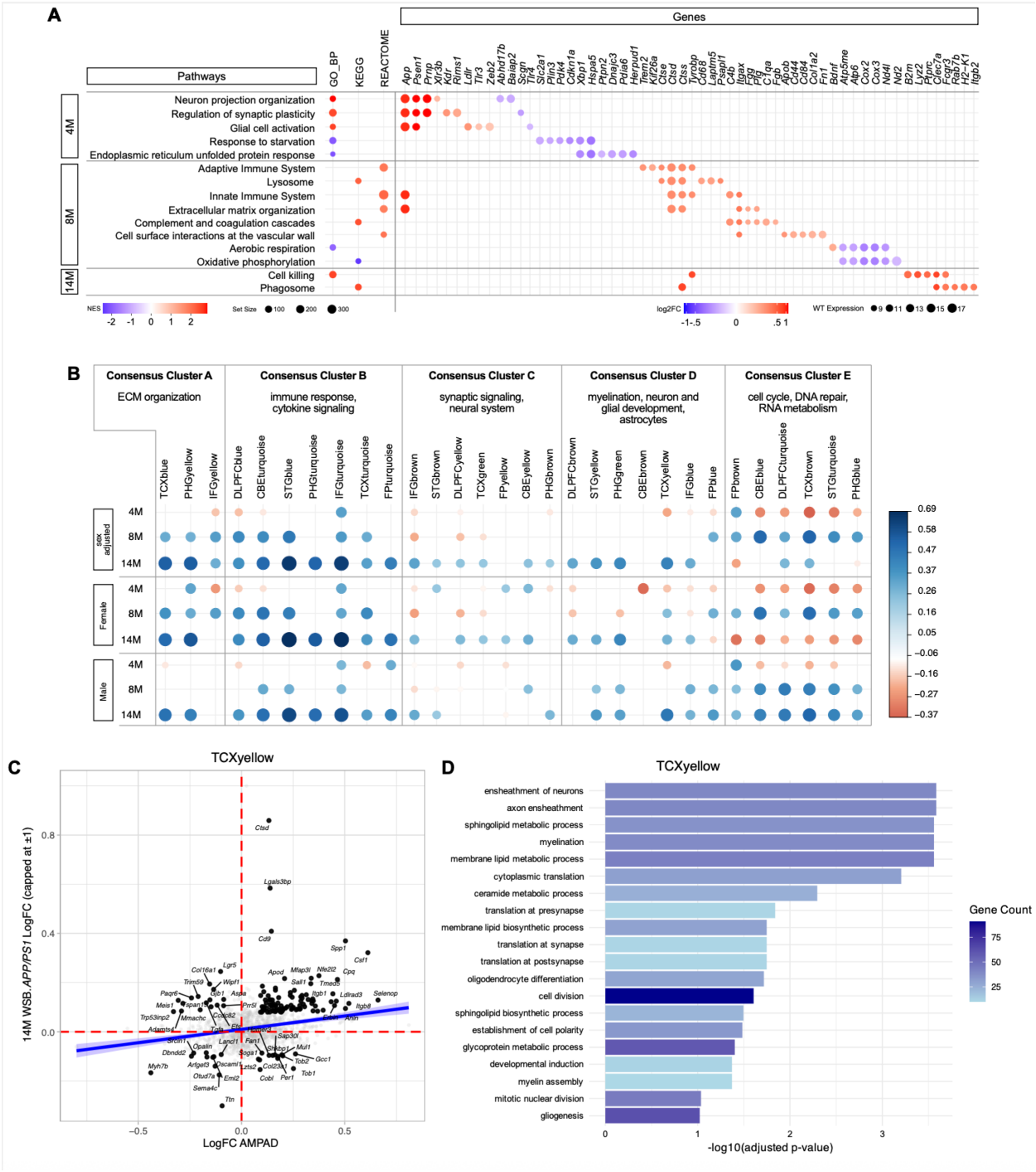

Figure 2: Transcritional profiling in WSB and WSB.APP/PS1 mice. **Gene set enrichment analysis in WSB.*APP/PS1* mice (compared to WSB) at 4, 8 and 14 months of age (M).** (**A**) Age-dependent pathways identified by GO, KEGG and Reactome. Genes relating to each pathway are shown to the right. For pathways, positive NES score are shown in red, negative NES scores are shown in blue. For genes, increased log2 fold change is shown in red, decreased log2 fold

change is shown in blue. (**B**) Alignment of differentially expressed genes in mouse with differentially expressed genes in human AMP-AD modules. A positive correlation is shown in blue, anti-correlation is shown in red. First three rows are combined for sex, second set of three rows are female only, third set of rows are male only. (**C**) One module, TCX yellow in Consensus Cluster D showed age-dependent correlations (strongest correlations at 14M), and included genes involved in microglia glia function on myelination. (**D**) Enrichment of genes positively correlated in human AMP-AD and WSB.*APP/PS1* mice identified myelination-related processes, predicting white matter changes.

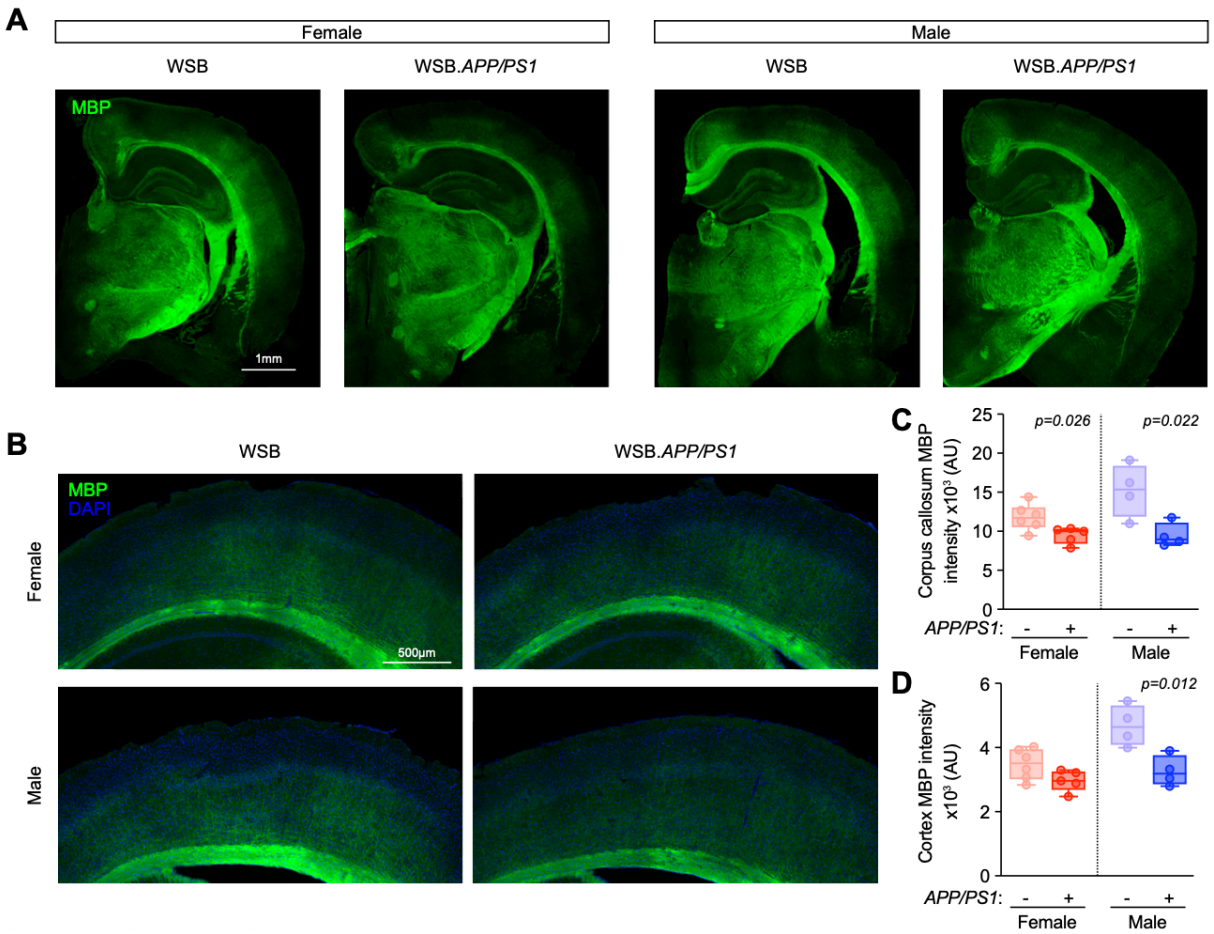

Figure 3: White matter changes in WSB.APP/PS1 mice compared to WSB WT mice. (**A**) Examples of sections from 14M male and female WSB WT and WSB.*APP/PS1* mice stained with myelin basic protein (MBP, green), a key component of white matter. (**B**) Examples of higher resolution images of the corpus callosum and cortex. (**C**) MBP intensity was quantified in four males and four females for each genotype at 14M. Male WSB.*APP/PS1* showed a significant reduction in MBP intensity in both the corpus callosum and the cortex (p=0.026 and p=0.012, respectively; two-tailed T tests). Female WSB.APP/PS1 mice showed a significant reduction in MBP intensity in the corpus callosum (p=0.026, two-tailed T test) and only showed a trend in reduced MBP intensity (p=0.072, two-tailed T-test). n=4 per sex per genotype.

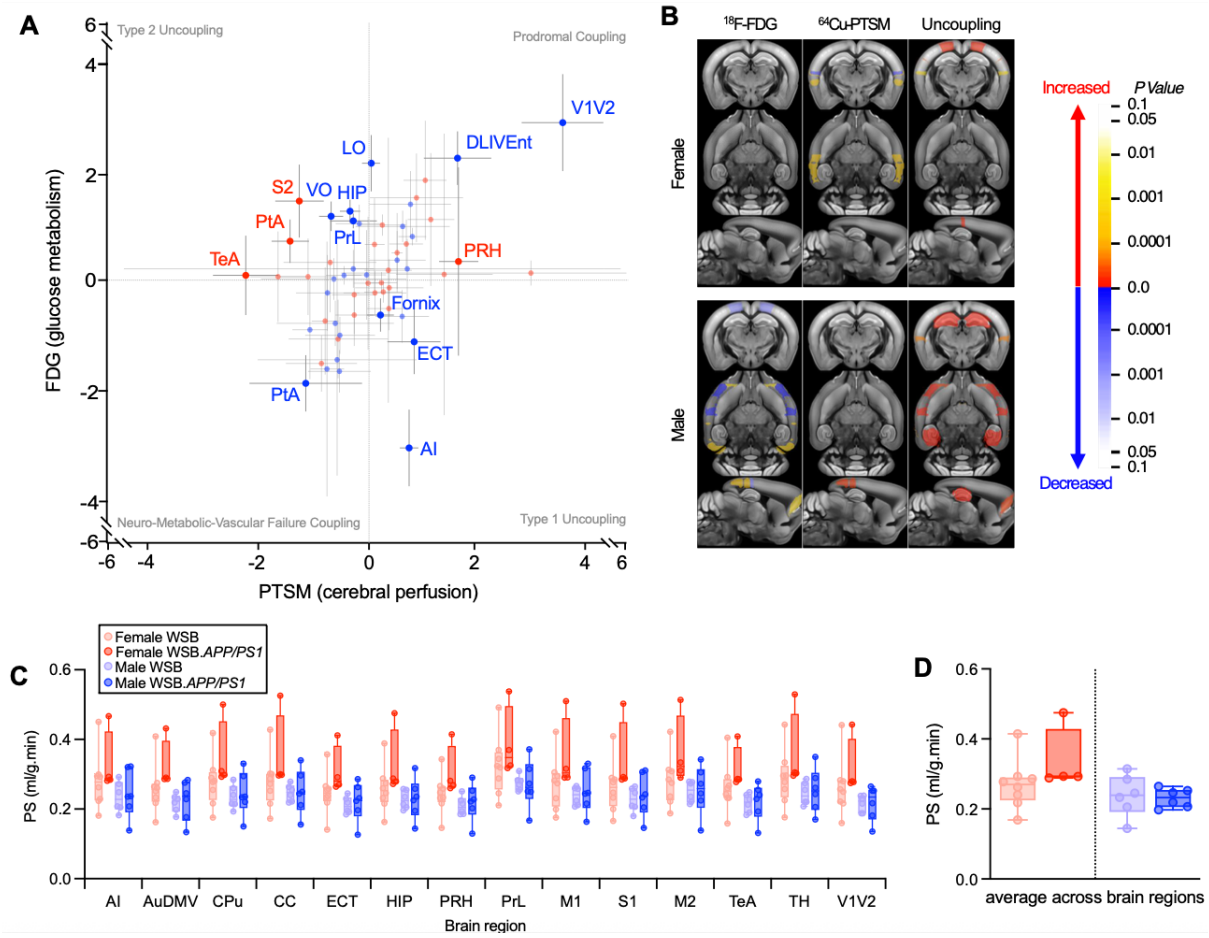

Figure 4: Uncoupling analysis in WSB and WSB.APP/PS1 mice.

(**A**) Neurovascular and metabolic uncoupling chart of WSB.APP/PS1 relative to WSB mice. As anticipated, WSB mice showed significant regional vascular and metabolic dysregulation with males and females showing 12/28 in Type 1 and Type 2 Uncoupling, and the majority of the regions in Prodromal (M/F = 7/11). (**B**) Spatially localized significant regions ($p < 0.05$). Significant regions were projected onto the Allen object maps to determine their spatial localization. The directionality of the change was indicated by applying the sign of the z-score to the p-value. Changes in vascular permeability (P) and surface area (S) across (**C**) brain regions and (**D**) whole brain. Female WSB.APP/PS1 mice showed a significant increase in PS product (regions $p<0.001$) relative to WSB mice across all brain regions. Male mice did not show this effect. These results highlight a sex-dimorphism alteration. Whole brain regional changes also showed the same genotype and sex effect.

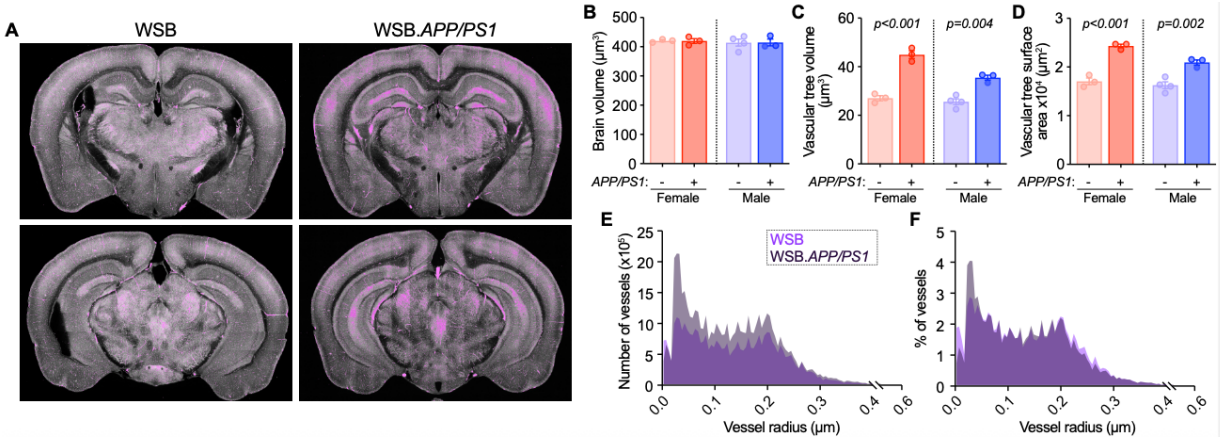

Figure 5: Characterization of extracted vascular tree in WSB and WSB.APP/PS1 mice. (**A**) 2D view of the extracted vascular tree for a WSB and WSB.APP/PS1. In the case of the WSB.APP/PS1, there is a noticeable increase in voxels detected as (**B**) measured brain volume, (**C**) vascular tree volume and (**D**) vascular tree surface area for the whole brain. Female WSB.APP/PS1 showed the greatest increase in both vasculature tree volume (female: $p<0.001$, male: $p=0.004$; two-tailed T tests) and surface area (female: $p<0.001$, male: $p=0.002$, two-tailed T tests). This is a powerful took to relate back to regions identified as significantly different based upon ^{64}Cu-PTSM PET/CT. Histogram of the measured vessel radius in: (**E**) mm and (**F**) percentages. The increase in volume and surface area appears to be driven by an increase in capillaries and meta-arterioles. The distributions shown are representative cases of female WSB WT and WSB.APP/PS1. The peak distribution in the WSB.APP/PS1 indicates an increased likelihood of small vessels like capillaries and meta-arterioles. While this initial increase in amyloid carriers may seem protective, the quality of these vessels remains to be determined.

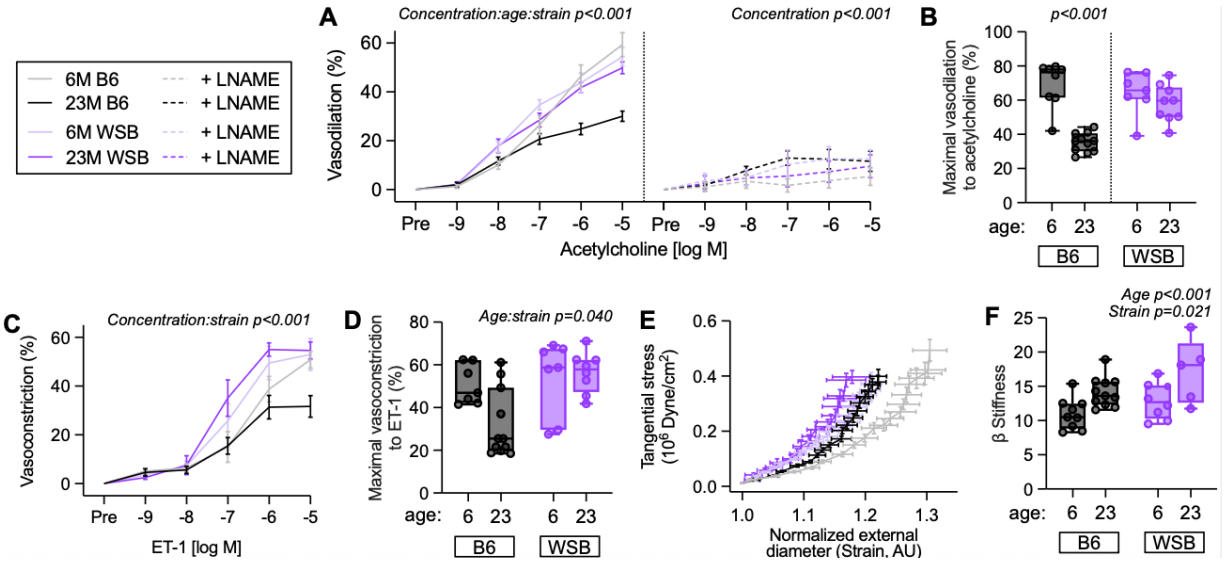

Figure 6: WSB mice do not have age-related impairments in cerebral artery vasoreactivity, but do have age-related elevations in cerebral artery stiffness.

Isolated posterior cerebral arteries were studied from 6M and 23M C57BL6J (B6) and WSB/EiJ (WSB) female mice. The vasodilation to endothelium-dependent dilator acetylcholine, displayed as (**A**) dose-response and (**B**) maximal vasodilation, was measured. There was a significant interaction among acetylcholine concentration, strain, and age ($p<0.001$, three-way ANOVA), but neither strain nor age modified the effect of acetylcholine concentration with the addition of L-name (concentration effect: $p<0.001$, three-way ANOVA). B6 mice had a significantly reduced maximal dilation response with age ($p<0.001$, Mann Whitney test), but WSB mice did not ($p=0.307$, two-tailed t test) (note: strains were analyzed separately due to non-normal distribution). (**C**) Dose-response and (**D**) maximal vasoconstriction to endothelin-1 (ET-1). Strain significantly modified the effect of endothelin concentration on vasoconstriction (Strain:concentration effect: $p<0.001$, three-way ANOVA). Strain significantly modified maximal vasoconstriction to ET-1 with age (age:strain effect: $p=0.040$, two-way ANOVA with Tukey's multiple comparison test). B6 mice had significantly diminished maximal vasoconstriction to ET-1 with age ($p=0.046$), which was not observed in WSB mice ($p=0.983$). Aged WSB mice had significantly higher maximal vasoconstriction compared to aged B6 mice two-way ANOVA ($p=0.004$). (**E**) Stress-strain curve used to calculate (**F**) β stiffness. Both age and strain significantly modified β stiffness (Age effect: $p<0.001$, strain effect: $p=0.021$ respectively, two-way ANOVA), but strain did not modify age-induced effects on β stiffness (Age:Strain effect; $p=0.5988$, two-way ANOVA).

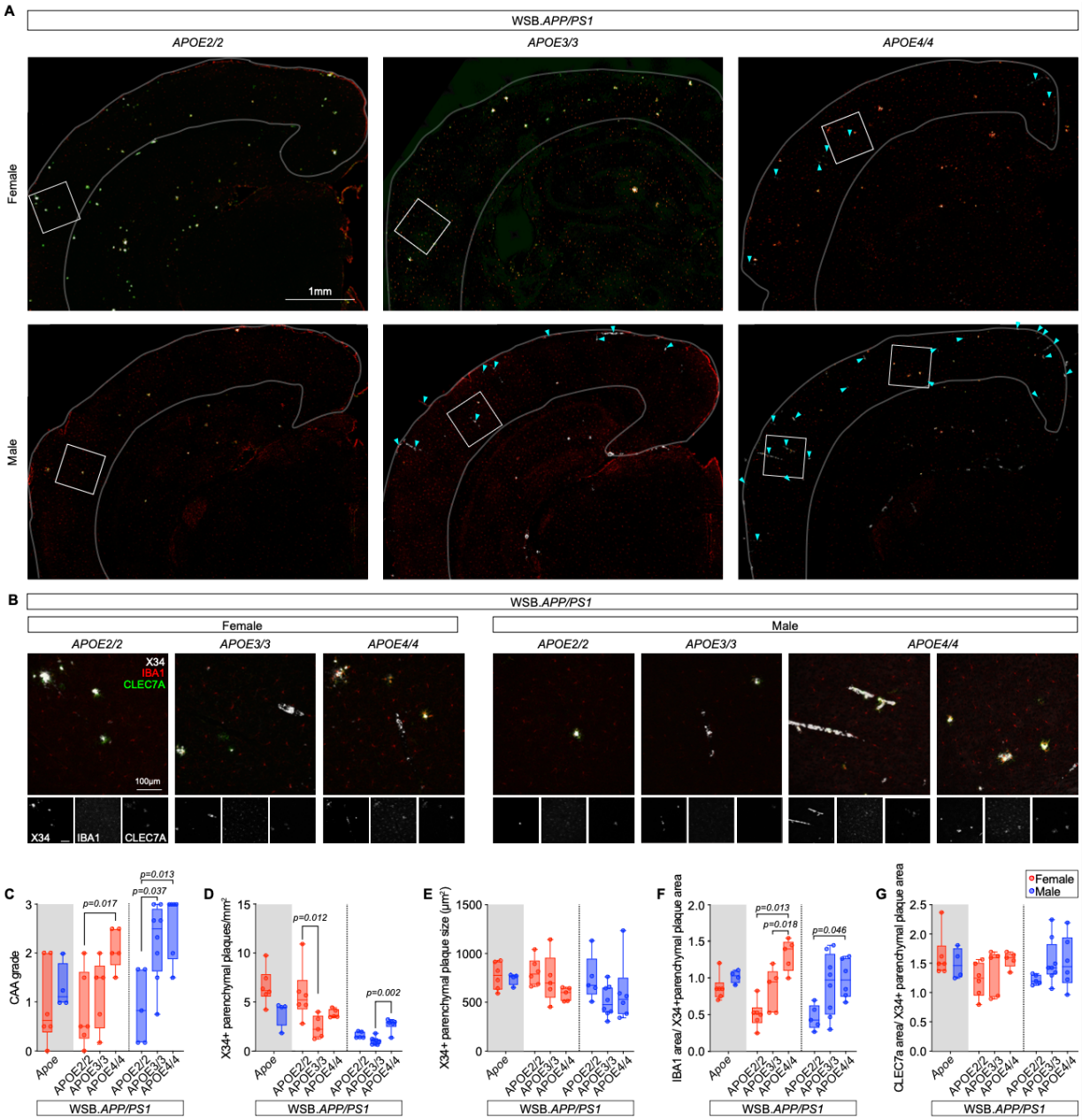

***Figure 7: CAA and parenchymal plaque characterization in WSB.APP/PS1 mice* with *APOE2/2*, *APOE3/3*, and *APOE4/4* alleles**

(A) Female and male 8M WSB.*APP/PS1;APOE2/2*, WSB.*APP/PS1;APOE3/3,* and WSB.*APP/PS1;APOE4/4* brain hemisections stained with X34 (white) and immunoassayed for IBA1(red) and CLEC7a (green). Arrowheads indicate CAA. **(B)** High-resolution insets of representative parenchymal plaques and CAA. Individual images of X34, IBA1, and CLEC7a are shown below the merged image. **(C)** Quantification of CAA scores. *APOE* genotype significantly influenced CAA in both females (p=0.020, one-way ANOVA, Tukey's multiple comparisons test)

and males (p=0.005, Brown-Forsythe ANOVA test, Dunnett's T3 multiple comparisons test). **(D)** Cortical parenchymal X34+ plaque quantifications normalized to cortical area. APOE genotype significantly influenced plaque number in both females and males (p=0.008 and p>0.001 respectively, Kruskal-Wallis tests with Dunn's multiple comparisons tests). **(E)** Average plaque size quantifications. No differences were observed in either sex across ages (female: p=0.113, one-way ANOVA; male: p=0.150, Kruskal-Wallis test). **(F)** Average IBA1+ area and CLEC7A+ area **(G)** normalized to average plaque size. APOE genotype significantly influenced IBA1+ area in both females and males (p<0.001 and p=0.039 respectively, one-way ANOVAs, Tukey's multiple comparisons tests). No differences were observed for CLEC7A+ area (female: p=0.197, one-way ANOVA; male: p=0.514, Brown-Forsythe ANOVA test). For WSB.*APP/PS1;APOE2/2*, WSB.*APP/PS1;APOE3/3*, and WSB.*APP/PS1;APOE4/4*, respectively; female: n=6, 5, 5; male: n=5, 8, 6. Data highlighted in gray are recapitulated from respective 8M WSB.*APP/PS1* measurements reported in Figure 1 (all of which had WT mouse *Apoe* genotypes) and were not statistically analyzed alongside WSB.*APP/PS1;APOE*/** data as they we generated separately.

Table 1. Posterior cerebral artery characteristics for ex vivo studies

Variable	Young B6	Old B6	Young WSB	Old WSB
Maximal Diameter (μm)	148 ± 1	150 ± 4	135 ± 6	144 ± 5
Maximal SNP dilation (%)	95 ± 2	83 ± 4	90 ± 3	91 ± 5
Preconstriction (%)				
ACh	24 ±2	22 ± 2	21 ±1	18 ± 2
ACh + LNAME	42 ± 5	37 ± 4	28 ± 4	30 ± 1
SNP	36 ± 5	27 ± 1	35 ± 4	33 ± 3

Data are mean ± SEM. ACh, acetylcholine; SNP, sodium nitroprusside. No statistical differences between groups (all $p>0.05$).

REFERENCES

1. A. Eid, I. Mhatre, J. R. Richardson, Gene-environment interactions in Alzheimer's disease: A potential path to precision medicine. *Pharmacol Ther* **199**, 173–187 (2019).
2. L. T. Grinberg, D. R. Thal, Vascular pathology in the aged human brain. *Acta Neuropathol* **119**, 277–290 (2010).
3. J. A. K. C. Chie *et al.*, Neuro-Metabolic and Vascular Dysfunction as an Early Diagnostic for Alzheimer's Disease and Related Dementias. *bioRxiv*, 2025.2005.2012.653558 (2025).
4. K. D. Onos *et al.*, Assessment of neurovascular uncoupling: APOE status is a key driver of early metabolic and vascular dysfunction. *Alzheimers Dement* **20**, 4951–4969 (2024).
5. A. Biffi, S. M. Greenberg, Cerebral amyloid angiopathy: a systematic review. *J Clin Neurol* **7**, 1–9 (2011).
6. K. D. Onos, S. J. Sukoff Rizzo, G. R. Howell, M. Sasner, Toward more predictive genetic mouse models of Alzheimer's disease. *Brain Res Bull* **122**, 1–11 (2016).
7. S. E. Heuer *et al.*, Control of hippocampal synaptic plasticity by microglia-dendrite interactions depends on genetic context in mouse models of Alzheimer's disease. *Alzheimers Dement* **20**, 601–614 (2024).
8. K. D. Onos *et al.*, Enhancing face validity of mouse models of Alzheimer's disease with natural genetic variation. *PLoS Genet* **15**, e1008155 (2019).
9. H. S. Yang *et al.*, Natural genetic variation determines microglia heterogeneity in wild-derived mouse models of Alzheimer's disease. *Cell Rep* **34**, 108739 (2021).
10. G. A. Churchill, D. M. Gatti, S. C. Munger, K. L. Svenson, The Diversity Outbred mouse population. *Mamm Genome* **23**, 713–718 (2012).
11. D. W. Threadgill, D. R. Miller, G. A. Churchill, F. P. de Villena, The collaborative cross: a recombinant inbred mouse population for the systems genetic era. *ILAR J* **52**, 24–31 (2011).
12. K. E. Foley *et al.*, APOE epsilon4 and exercise interact in a sex-specific manner to modulate dementia risk factors. *Alzheimers Dement (N Y)* **8**, e12308 (2022).
13. O. J. Marola *et al.*, Genetic context modulates aging and degeneration in the murine retina. *Mol Neurodegener* **20**, 8 (2025).
14. A. M. Reagan *et al.*, The 677C > T variant in methylenetetrahydrofolate reductase causes morphological and functional cerebrovascular deficits in mice. *J Cereb Blood Flow Metab* **42**, 2333–2350 (2022).
15. G. W. Zack, W. E. Rogers, S. A. Latt, Automatic measurement of sister chromatid exchange frequency. *J Histochem Cytochem* **25**, 741–753 (1977).
16. K. P. Kotredes *et al.*, Characterizing molecular and synaptic signatures in mouse models of late-onset Alzheimer's disease independent of amyloid and tau pathology. *Alzheimers Dement* **20**, 4126–4146 (2024).
17. B. Li, C. N. Dewey, RSEM: accurate transcript quantification from RNA-Seq data with or without a reference genome. *BMC Bioinformatics* **12**, 323 (2011).
18. S. Anders, P. T. Pyl, W. Huber, HTSeq--a Python framework to work with high-throughput sequencing data. *Bioinformatics* **31**, 166–169 (2015).
19. A. Subramanian *et al.*, Gene set enrichment analysis: a knowledge-based approach for interpreting genome-wide expression profiles. *Proc Natl Acad Sci U S A* **102**, 15545–15550 (2005).

20. Y. W. Wan *et al.*, Meta-Analysis of the Alzheimer's Disease Human Brain Transcriptome and Functional Dissection in Mouse Models. *Cell Rep* **32**, 107908 (2020).
21. M. Allen *et al.*, Human whole genome genotype and transcriptome data for Alzheimer's and other neurodegenerative diseases. *Sci Data* **3**, 160089 (2016).
22. P. L. De Jager *et al.*, A multi-omic atlas of the human frontal cortex for aging and Alzheimer's disease research. *Sci Data* **5**, 180142 (2018).
23. M. Wang *et al.*, The Mount Sinai cohort of large-scale genomic, transcriptomic and proteomic data in Alzheimer's disease. *Sci Data* **5**, 180185 (2018).
24. M. Sasner *et al.*, In vivo validation of late-onset Alzheimer's disease genetic risk factors. *Alzheimers Dement* **20**, 4970–4984 (2024).
25. M. A. Green, A potential copper radiopharmaceutical for imaging the heart and brain: copper-labeled pyruvaldehyde bis(N4-methylthiosemicarbazone). *Int J Rad Appl Instrum B* **14**, 59–61 (1987).
26. C. J. Mathias *et al.*, In vivo comparison of copper blood-pool agents: potential radiopharmaceuticals for use with copper-62. *J Nucl Med* **32**, 475–480 (1991).
27. L. Sokoloff, Relation between physiological function and energy metabolism in the central nervous system. *J Neurochem* **29**, 13–26 (1977).
28. S. Krishnamoorthy *et al.*, Performance evaluation of the MOLECUBES beta-CUBE-a high spatial resolution and high sensitivity small animal PET scanner utilizing monolithic LYSO scintillation detectors. *Physics in medicine and biology* **63**, 155013 (2018).
29. C. Studholme, D. L. Hill, D. J. Hawkes, Automated three-dimensional registration of magnetic resonance and positron emission tomography brain images by multiresolution optimization of voxel similarity measures. *Med Phys* **24**, 25–35 (1997).
30. K. B. J. Franklin, G. Paxinos, *Paxinos and Franklin's The mouse brain in stereotaxic coordinates*. (Academic Press, an imprint of Elsevier, Amsterdam, ed. Fourth edition., 2013), pp. 1 volume (unpaged).
31. K. Shimoji *et al.*, Measurement of cerebral glucose metabolic rates in the anesthetized rat by dynamic scanning with 18F-FDG, the ATLAS small animal PET scanner, and arterial blood sampling. *J Nucl Med* **45**, 665–672 (2004).
32. L. Sokoloff *et al.*, The [14C]deoxyglucose method for the measurement of local cerebral glucose utilization: theory, procedure, and normal values in the conscious and anesthetized albino rat. *J Neurochem* **28**, 897–916 (1977).
33. H. Toyama *et al.*, Absolute quantification of regional cerebral glucose utilization in mice by 18F-FDG small animal PET scanning and 2-14C-DG autoradiography. *J Nucl Med* **45**, 1398–1405 (2004).
34. G. D. Hutchins *et al.*, Alternative approach to single-scan estimation of cerebral glucose metabolic rate using glucose analogs, with particular application to ischemia. *J Cereb Blood Flow Metab* **4**, 35–40 (1984).
35. M. E. Phelps *et al.*, Tomographic measurement of local cerebral glucose metabolic rate in humans with (F-18)2-fluoro-2-deoxy-D-glucose: validation of method. *Ann Neurol* **6**, 371–388 (1979).
36. D. Xia *et al.*, Novel App knock-in mouse model shows key features of amyloid pathology and reveals profound metabolic dysregulation of microglia. *Mol Neurodegener* **17**, 41 (2022).
37. Q. Wang *et al.*, The Allen Mouse Brain Common Coordinate Framework: A 3D Reference Atlas. *Cell* **181**, 936–953 e920 (2020).

38. T.-C. Lee, R. L. Kashyap, C.-N. Chu, Building skeleton models via 3-D medial surface axis thinning algorithms. *CVGIP: graphical models and image processing* **56**, 462–478 (1994).
39. E. H. Reeve *et al.*, Pyridoxamine treatment ameliorates large artery stiffening and cerebral artery endothelial dysfunction in old mice. *J Cereb Blood Flow Metab* **43**, 281–295 (2023).
40. A. E. Walker *et al.*, Cerebral and skeletal muscle feed artery vasoconstrictor responses in a mouse model with greater large elastic artery stiffness. *Exp Physiol* **104**, 434–442 (2019).
41. E. Spangenberg *et al.*, Sustained microglial depletion with CSF1R inhibitor impairs parenchymal plaque development in an Alzheimer's disease model. *Nat Commun* **10**, 3758 (2019).
42. C. Hetz, K. Zhang, R. J. Kaufman, Mechanisms, regulation and functions of the unfolded protein response. *Nat Rev Mol Cell Biol* **21**, 421–438 (2020).
43. H. Keren-Shaul *et al.*, A Unique Microglia Type Associated with Restricting Development of Alzheimer's Disease. *Cell* **169**, 1276–1290 e1217 (2017).
44. S. Wang, X. Lai, Y. Deng, Y. Song, Correlation between mouse age and human age in anti-tumor research: Significance and method establishment. *Life Sci* **242**, 117242 (2020).
45. W. E. Van Nostrand, J. P. Melchor, G. Romanov, K. Zeigler, J. Davis, Pathogenic effects of cerebral amyloid angiopathy mutations in the amyloid beta-protein precursor. *Ann N Y Acad Sci* **977**, 258–265 (2002).
46. G. Blazhenets *et al.*, Principal Components Analysis of Brain Metabolism Predicts Development of Alzheimer Dementia. *J Nucl Med* **60**, 837–843 (2019).
47. D. A. Butterfield, B. Halliwell, Oxidative stress, dysfunctional glucose metabolism and Alzheimer disease. *Nat Rev Neurosci* **20**, 148–160 (2019).
48. J. Yao, J. R. Rettberg, L. P. Klosinski, E. Cadenas, R. D. Brinton, Shift in brain metabolism in late onset Alzheimer's disease: implications for biomarkers and therapeutic interventions. *Mol Aspects Med* **32**, 247–257 (2011).
49. Y. Iturria-Medina *et al.*, Early role of vascular dysregulation on late-onset Alzheimer's disease based on multifactorial data-driven analysis. *Nat Commun* **7**, 11934 (2016).
50. M. D. Sweeney *et al.*, Vascular dysfunction-The disregarded partner of Alzheimer's disease. *Alzheimers Dement* **15**, 158–167 (2019).
51. L. L. Beason-Held *et al.*, Changes in brain function occur years before the onset of cognitive impairment. *J Neurosci* **33**, 18008–18014 (2013).
52. L. L. Chao *et al.*, ASL perfusion MRI predicts cognitive decline and conversion from MCI to dementia. *Alzheimer Dis Assoc Disord* **24**, 19–27 (2010).
53. S. M. Kim *et al.*, Regional cerebral perfusion in patients with Alzheimer's disease and mild cognitive impairment: effect of APOE epsilon4 allele. *Neuroradiology* **55**, 25–34 (2013).
54. A. Boroujerdi, J. V. Welser-Alves, U. Tigges, R. Milner, Chronic cerebral hypoxia promotes arteriogenic remodeling events that can be identified by reduced endoglin (CD105) expression and a switch in beta1 integrins. *J Cereb Blood Flow Metab* **32**, 1820–1830 (2012).
55. M. I. Cybulsky, P. A. Marsden, Effect of disturbed blood flow on endothelial cell gene expression: a role for changes in RNA processing. *Arterioscler Thromb Vasc Biol* **34**, 1806–1808 (2014).

56. A. S. Salinet *et al.*, Impaired cerebral autoregulation and neurovascular coupling in middle cerebral artery stroke: Influence of severity? *J Cereb Blood Flow Metab* **39**, 2277–2285 (2019).
57. A. Seiler *et al.*, The relationship between blood flow impairment and oxygen depletion in acute ischemic stroke imaged with magnetic resonance imaging. *J Cereb Blood Flow Metab* **39**, 454–465 (2019).
58. A. Salehi, J. H. Zhang, A. Obenaus, Response of the cerebral vasculature following traumatic brain injury. *J Cereb Blood Flow Metab* **37**, 2320–2339 (2017).
59. J. Attems, M. Quass, K. A. Jellinger, F. Lintner, Topographical distribution of cerebral amyloid angiopathy and its effect on cognitive decline are influenced by Alzheimer disease pathology. *J Neurol Sci* **257**, 49–55 (2007).
60. H. K. Lee, S. J. Widmayer, M. N. Huang, D. L. Aylor, D. A. Marchuk, Novel Neuroprotective Loci Modulating Ischemic Stroke Volume in Wild-Derived Inbred Mouse Strains. *Genetics* **213**, 1079–1092 (2019).
61. M. V. Donoso *et al.*, Aging differentially modifies arterial sensitivity to endothelin-1 and 5-hydroxytryptamine: studies in dog coronary arteries and rat arterial mesenteric bed. *Peptides* **15**, 1489–1495 (1994).
62. W. G. Mayhan, D. M. Arrick, G. M. Sharpe, H. Sun, Age-related alterations in reactivity of cerebral arterioles: role of oxidative stress. *Microcirculation* **15**, 225–236 (2008).
63. M. L. Modrick, S. P. Didion, C. D. Sigmund, F. M. Faraci, Role of oxidative stress and AT1 receptors in cerebral vascular dysfunction with aging. *Am J Physiol Heart Circ Physiol* **296**, H1914–1919 (2009).
64. R. D. Shipley, J. M. Muller-Delp, Aging decreases vasoconstrictor responses of coronary resistance arterioles through endothelium-dependent mechanisms. *Cardiovasc Res* **66**, 374–383 (2005).
65. A. J. Donato *et al.*, Vascular endothelial dysfunction with aging: endothelin-1 and endothelial nitric oxide synthase. *Am J Physiol Heart Circ Physiol* **297**, H425–432 (2009).
66. A. V. Kuczmarski, L. M. Welti, K. L. Moreau, M. M. Wenner, ET-1 as a Sex-Specific Mechanism Impacting Age-Related Changes in Vascular Function. *Front Aging* **2**, 727416 (2021).
67. A. L. Jefferson *et al.*, Higher Aortic Stiffness Is Related to Lower Cerebral Blood Flow and Preserved Cerebrovascular Reactivity in Older Adults. *Circulation* **138**, 1951–1962 (2018).
68. A. E. Walker *et al.*, Greater impairments in cerebral artery compared with skeletal muscle feed artery endothelial function in a mouse model of increased large artery stiffness. *J Physiol* **593**, 1931–1943 (2015).
69. B. T. Kress *et al.*, Impairment of paravascular clearance pathways in the aging brain. *Ann Neurol* **76**, 845–861 (2014).
70. J. J. Iliff *et al.*, A paravascular pathway facilitates CSF flow through the brain parenchyma and the clearance of interstitial solutes, including amyloid beta. *Sci Transl Med* **4**, 147ra111 (2012).
71. J. L. Cummings *et al.*, Alzheimer's disease drug development pipeline: 2025. *Alzheimers Dement (N Y)* **11**, e70098 (2025).
72. K. E. Foley, D. M. Wilcock, Vascular Considerations for Amyloid Immunotherapy. *Curr Neurol Neurosci Rep* **22**, 709–719 (2022).

73. A. L. Oblak *et al.*, Model organism development and evaluation for late-onset Alzheimer's disease: MODEL-AD. *Alzheimers Dement (N Y)* **6**, e12110 (2020).